APPENDIX - TABLE OF CONTENTS

1. Appendix Supplementary Materials and methods

Generation of HeLa cell lines - AcGFP1 is an inert monomeric fluorescent protein derived from *Aequorea coerulescens*, the intense illumination of which is not phototoxic (**Bulina *et al.*, 2006; Bell *et al.*, 2007; Dieteren *et al.*, 2008; Dieteren *et al.*, 2011**). HeLa cell lines stably expressing AcGFP1 or AcGFP^2 were generated using the same vector constructs as described previously for HEK293 cells (**Dieteren *et al.*, 2008**). To this end, cDNA of the cox8 leader sequence (first 210 base pairs of sequence NM_00004074) was generated by Gateway-adapted PCR procedures according to the manufacturer's instructions (**Invitrogen Thermo Fisher, Carlsbad, CA, USA**). A cox8-entry clone was generated from the resulting PCR product by recombination with pDONR201 (**Invitrogen**) using Gateway Clonase II Enzyme Mix (**Invitrogen**). An AcGFP1 destination vector was generated by subcloning the BamHI/NotI restriction fragment of pAcGFP1-N1 (**Clontech, Westburg, Leusden, The Netherlands**) in-frame behind Gateway Reading Frame Cassette B (**Invitrogen**) in pcDNA5/FRT/TO (**Invitrogen**). To obtain an inducible vector containing mitochondrial matrix-targeted AcGFP1, the entry vector was recombined with the AcGFP1 destination vector by using Gateway LR Clonase II Enzyme Mix (**Invitrogen**). In the same manner, a tandem mitochondrial AcGFP1 expression vector (AcGFP1^2) was created by first generating an entry vector containing the cox8 leader sequence linked to the N-terminus of AcGFP1 (without the stop codon) and then recombining this entry clone with the AcGFP1-destination vector. To create a cox8-cox8-AcGFP1 entry clone, the cox8- sequence of the cox8-AcGFP1 entry clone was replaced by a cox8-cox8 sequence amplified from a "Pericam" vector (**Palmer *et al.*, 2004**) using the primers: Fwd_5'aaatttaaaGGGCCCCAAATAATGATTTTATTTTGA3' and Rev_5'ataataataACCGGTTTGAGATCTCCCTCCGGCGGCAA3' using the ApaI and AgeI restriction sites for ligation. Accuracy of the vector was confirmed by sequencing. To create a triple AcGFP1 expression vector (AcGFP1^3), an AcGFP1^3 destination vector was generated by consecutive cloning steps. First, an AcGFP1 fragment was generated by PCR using the primers Fwd_5'tatataACCGGTATCGATaaaattGCTAGCcatggtgagcaagggcgccgag3' and Rev_5'tatataaccggtA TGCATaacaatt gGATATCcttgtacagctcatccatgcc3' on pAcGFP-N1 (**Clontech**) as a template, and ligated into the AgeI site of the AcGFP1 destination vector, delivering an AcGFP1^2 destination vector. Subsequently, the cox8-cox8-AcGFP1 entry clone was recombined with this AcGFP1^2 destination vector using Gateway LR Clonase II Enzyme mix (**Invitrogen**), generating a cox8-cox8-AcGFP1^3 expression vector. Unfortunately, this expression vector displayed suboptimal mitochondrial expression (data not shown). As an alternative strategy, an AcGFP1 fragment was generated by PCR with primers Fwd_5'ttt tttGATATCcCGCCGCACCCAGCTTTCTTGT3' and Rev_5'ttttttATGCATgTCGATACCG GTGGATCATCAAC3' with cox8-cox8-AcGFP1^3 expression vector as template, and ligated into the EcoRV and NsiI sites of the AcGFP1^2 destination vector. This AcGFP1^3 destination vector was recombined with the cox8-entry vector and the cox8-cox8-AcGFP1 entry vector using Gateway LR Clonase II Enzyme mix (**Invitrogen**), generating the AcGFP1^3 and AcGFP1^4 expression vectors used further in this study, respectively. HeLa T-REx Flp-in cells were stably transfected using Superfect Transfection Reagent (**Qiagen, Venlo, The Netherlands**) according to the manufacturer's protocol and cultured for selection in the presence of 200 µg/ml hygromycin (#10687010; **Invitrogen**) in Dulbecco's modified Eagle's medium (DMEM; #31966; **Gibco Thermo-Fisher, MD, Gaithersburg, USA**) supplemented with 10% (v/v) fetal bovine serum (#10270; **Gibco**), 1% (v/v) penicillin/streptomycin (#15140; **Gibco**) and 4 µg/ml blasticin (# R21001; **Gibco**). The DMEM also contained 25 mM D-glucose, 3.97 mM L-Alanyl-L-Glutamine (GlutaMAX) and 1 mM pyruvate. Parental cells were cultured in the presence of 50 µg/ml zeocin (#R25001; **Invitrogen**) instead of hygromycin. All cell lines were tested for mycoplasma contamination and found negative.

Mitochondrial colocalization analysis - HeLa cells were cultured on glass-bottomed WillCo® dishes (**WillCo Wells B.V., Amsterdam, The Netherlands**) and induced with doxycycline (1 µg/ml; 24 h). Next, the cells were incubated with 1 µM MitoTracker Red CM-H2XROS (#M7513; **Invitrogen)** for 30 min in the dark (37º, 95% air, 5% CO_2). Then, the cells were washed with a colourless HEPES-Tris (HT) solution

(132 mM NaCl, 4.2 mM KCl, 1 mM $CaCl_2$, 1 mM $MgCl_2$, 5.5 mM D-glucose and 10 mM HEPES, pH 7.4) and fluorescence microscopy images were acquired using a ZEISS LSM510 Meta confocal microscope (**Carl Zeiss B.V., Sliedrecht, The Netherlands**) using a Plan-Apochromat 63x/1.40 Oil DIC objective (**Carl Zeiss**), a zoom factor of 2 and an optical slice thickness of < 1 µm. AcGFP1 and MitoTracker Red fluorescence signals were collected following excitation at 488 nm (Argon laser; set at 2% transmission) and 543 nm (Helium/Neon laser; 43% transmission), respectively. AcGFP1 fluorescence was detected using a 488nm dichroic mirror and a 500-530 nm band pass filter. MitoTracker Red fluorescence was detected using a 543 nm dichroic mirror and a 560 nm long pass filter.

Flowcytometry - HeLa T-REx Flp-in cells were cultured in 24-well plates (#662160; **Cellstar, Greiner Bio-One International GmbH, Alphen aan de Rijn, The Netherlands**). Using half of the wells, expression of AcGFP1 concatemers was induced with doxycycline (1 µg/ml; 24 h). Prior to flowcytometry measurements cells were trypsinized, washed with PBS and resuspended in colourless DMEM (#A14430-01; **Gibco**). Cells were analyzed using a FACSCalibur flow cytometer (**BD Biosciences, Alschwil, Switserland**) and data was exported to Excel using FloJo software.

Fluorescence recovery after photobleaching experiments - For FRAP analysis (*e.g.* **Lorén *et al.*, 2015**), cells were seeded in glass-bottomed WillCo® dishes (**WillCo Wells B.V., Amsterdam, The Netherlands)** and grown to ~70% confluence. As a reference, the cox8-AcGFP1-expressing cell line ("AcGFP1") was included on each day of experiments. Measurements were performed using a ZEISS LSM510 Meta confocal microscope (**Carl Zeiss**) at 20 ºC (293K) to minimize mitochondrial movement (**Koopman *et al.*, 2006; Dieteren *et al.*, 2008; Dieteren *et al.*, 2011**). Images were acquired at 10 Hz using a Plan-Apochromat 63x oil immersion objective (NA=1.4; **Carl Zeiss**). Pre- and post-bleach imaging was performed using 488 nm excitation light (Argon laser; set at 3% transmission), a 488 nm dichroic mirror and a 505 nm longpass filter. First the pre-bleach fluorescence level was recorded, after which AcGFP1 photobleaching was performed (Argon laser; set at 100% transmission for 100 ms) in a FRAP region of 10x10 pixels (measuring 1.4x1.4 µm). Routinely, a zoom factor of 4 was used and pinhole settings were chosen to achieve an optical thickness of < 2 µm. Only single mitochondria that were fully located within the focal plane were used for analysis (confirmed by an axial scan through the filament). Only mitochondria in which FRAP was paralleled by fluorescence loss in photobleaching (FLIP) in a part distal to the FRAP region were considered to possess a continuous mitochondrial matrix and included in the analysis (**Appendix Fig. S2A-B-C**). In our experiments the size of the FRAP region is relatively large when compared to the size of the mitochondrion. Therefore, the experimental FRAP curves (F(t)) were corrected as described previously (**Goodwin & Kenworthy, 2005; Dieteren *et al.*, 2011**) using:

$$F(t) = 100 \times \frac{(F(t)_{\text{FRAPregion}} - F(t)_{\text{background}})}{(F(t)_{\text{totalmito}} - F(t)_{\text{background}})} \times \frac{(F_{\text{i,totalmito}} - F_{\text{background}})}{(F_{\text{i,FRAPregion}} - F_{\text{background}})} \qquad \textbf{[Equation-I]}$$

Here the fluorescence intensity in the bleached mitochondrial region ($F(t)_{FRAPregion}$) and for the total mitochondrion ($F(t)_{totalmito}$), is background-corrected ($F(t)_{background}$) at each time point. Next, the corrected fluorescence signal in the bleached region is divided by the corrected intensity of the total mitochondrion to correct for the loss of mitochondrial fluorescence during the bleach. The corrected data are normalized to the background-corrected pre-bleach intensity ($F_{i,FRAP\ region}$ and $F_{i,total\ mito}$) and multiplied by 100 to yield a percentage of pre-bleach fluorescence (**Appendix Fig. S2**). Applying **[Equation-I]** also corrects for photobleaching induced by normal image acquisition. Mean fluorescence recovery curves were calculated by averaging multiple FRAP recordings from single mitochondria. This averaging improved the signal-to-noise ratio, which facilitated convergence of the Levenberg-Marquardt algorithm (**Levenberg, 1944**; **Marquardt, 1963**) used for fitting of the average FRAP curves with a mono-exponential equation (**Dieteren *et al.*, 2011**):

$$F(t) = y_0 + A_{mono}\left(1 - e^{-\frac{t}{T_{mono}}}\right) \quad \textbf{[Equation-II]}$$

With T_{mono} representing the FRAP time constant. The mobile fraction (F_m) was calculated from the average FRAP curves using:

$$F_m = \frac{F_\infty - F_0}{F_i - F_0} \quad \textbf{[Equation-III]}$$

With $F_\infty = y_0 + A_{mono}$ being the fluorescence intensity at $t = t_\infty$. F_0 equals the starting fluorescence level directly after the bleach pulse (as % of the pre-bleach value) and the pre-bleach fluorescence signal (F_i) is set at 100% (due to application of **[Equation I]**).

SDS-PAGE, in-gel fluorescence analysis and Western blotting of mitochondrial fractions - Cells were harvested by trypsinization, washed with cold PBS, centrifuged (5 min, 1000 g, 4˚C) and resuspended in 250 µL MSE buffer (225 mM mannitol, 75 mM D-sucrose and 1 mM Na-EDTA, pH 7.4) supplemented with 1x protease inhibitor cocktail (#05892791001; **Roche Diagnostics Merck**). Cells were exposed to three cycles of cold (liquid nitrogen) and heat shock (37˚C) and homogenized with a micro pestle. Cell debris was pelleted by centrifugation (15 min, 600 g, 4˚C). The supernatant was centrifuged at high speed in order to pellet mitochondria (15 min, 10,000 g, 4˚C). The mitochondrial pellet was dissolved in 40 µL PBS containing 2% (w/v) β-lauryl maltoside and incubated on ice for 10 minutes. Protein concentrations were determined using Protein Assay Dye Reagent Concentrate (#500-0006; **Bio-Rad Laboratories, Hercules, CA, USA**). Spectrophotometric absorbance was measured at 595 nm in a Benchmark Plus plate reader (**Bio-Rad**). Mitochondrial fractions were run on a 4-15% SDS-PAGE gel. First, the gel (40 µg protein per lane) was used for "in-gel" fluorescence analysis of AcGFP1 using a ChemiDoc MP imaging system (**Bio-Rad**). Next, the same gel was used for Western blotting and immunodetection using a rabbit polyclonal antibody against EGFP (kindly provided by F.J. van Kuppeveld, Dept. of Medical Microbiology, Radboudumc, The Netherlands) and a mouse monoclonal antibody against VDAC1 (#MABN504, 1:1000; **Merck**). Anti-rabbit IRDye800 and anti-mouse IRDye680 (**Li-cor Biosciences, Lincoln, NE, USA**) antibodies were used as secondary antibodies. Blots were scanned using an Odyssey CLx scanner (**Li-cor**).

SDS-PAGE and Western blotting of whole-cell lysates - Cells were harvested as described in the previous section. Cell pellets were resuspended in RIPA buffer (50 mM Tris-HCl (pH 7.4), 50 mM NaCl, 1% (v/v) Triton X-100, 5 mM Na_2EDTA, 10 mM $Na_4P_2O_7 \cdot 10H_2O$, 50 mM NaF, 1x Protease Inhibitor Cocktail (#05892791001; Roche), 1 x PhosStop (#04906845001; Roche) and 100 µg/mL DNase I (#79254; Qiagen)) and incubated on ice for 30 min and vortexed every 5 min. Debris was pelleted by centrifugation (10 min, 13.000 rpm, 4°C) and the supernatant was saved to serve as whole cell lysate. Protein concentrations were determined as described in the previous section. Whole-cell lysates (20-25 µg per lane) were run on a 4-15% SDS-PAGE gel and used for Western blotting and immunodetection using the following antibodies: Rabbit-anti-mtHSP60 (#NBP2-67517; **Novus Biologicals, Centennial, CO, USA**), Mouse-anti-mtHSP70/GRP75/HSPA9B/Mortalin (#NBP1-47801; **Novus**), Mouse-anti-LONP1 (#66043-1-Ig; **Proteintech Europe, Manchester, United Kingdom**), Mouse-anti-CLPP (#WH0008192M1; **Merck/Sigma-Aldrich Chemie N.V., Zwijndrecht, The Netherlands**), Rabbit-anti-CHOP/GADD153 (#NBP2-66856; **Novus**), Mouse-anti-OPA1 (#H00004976-M01; **Abnova, Taipei, Taiwan**), Mouse-anti-DRP1 (DLP1; #611112; **BD Transduction Lab**), Rabbit-anti-MFN2 (#m6444; **Sigma-Aldrich**), Mouse-anti-Porin (Porin/VDAC1; #MABN504; 35-kDa; **Merck Millipore**) and Mouse-anti-beta-actin (#A5441; **Sigma-Aldrich**). Blots were scanned using an Odyssey CLx scanner (**Li-cor**).

Oxygen consumption rate (OCR) and extracellular acidification rate (ECAR) measurements - On the day of measurement, a Cell Culture Microplate (#101085-004; **Agilent, Santa Clara, CA, USA**) was coated with Cell-Tak® (#734-1081; **BD Biosciences, San Jose, CA, USA**; 22.4 µg/ml in 0.1 M $NaHCO_3$) at 37˚C (non CO_2-corrected atmosphere) for at least 1 h. Next, cells were seeded at a density of 30,000

cells/well (6 replicates for each condition) in non pH-buffered Seahorse medium (DMEM containing 2 mM glutamine, 11 mM D-(+)glucose and 1 mM pyruvate; pH set to 7.4 with NaOH). Next, the plates were placed in an incubator without CO_2 correction for 1 h at 37°C. Using a Seahorse® XFe96 Analyzer (**Agilent**), the oxygen consumption rate (OCR) and extracellular acidification rate (ECAR) were measured for each well. Basal OCR/ECAR was quantified using three cycles (each consisting of 3 min of mixing followed by 3 min of recording). A similar approach was used to subsequently quantify the effects of 1 µM oligomycin (OLI; #75351; **Sigma**), two additions (2 µM and 1 µM) of carbonyl cyanide-p-trifluoromethoxyphenylhydrazone (FCCP; #C2920; **Sigma**) and the combined addition of 1.25 µM rotenone (ROT; #R887; **Sigma**) and 2.5 µM antimycin A (AA; #A8674; **Sigma**). Individual wells with zero OCR values and the corresponding ECAR data points were excluded from the analysis.

TMRM measurements **-** Cells were seeded at a density of 10,000/dish (FluoroDishes®; #FD35-100; **World Precision Instruments Ltd., Friedberg Germany**). Following 24 h of culturing, the DMEM medium was replaced by DMEM containing 40 µg/ml chloramphenicol (CAP; #C0378; **Sigma**). Prior to microscopy analysis, cells were incubated (in the dark; humidified atmosphere; 95% air; 5% CO_2, 25 min, 37°C) with 15 nM tetramethylrhodamine methyl ester (TMRM; #T668; **Life Technologies Thermo Fisher Scientific, Waltham, MA, USA**) diluted from a DMSO-dissolved stock solution. Directly following this incubation, the cells were placed on the stage of a fully motorized inverted microscope (**Carl Zeiss**; described in detail elsewhere: **Nooteboom *et al.*, 2012**). Fluorescence images were acquired within 15 min after incubation in the continuous presence of 15 nM extracellular TMRM using an 40x/1.3 NA Plan NeoFluar objective (**Carl Zeiss**), 540 nm excitation light delivered by a monochromator (**TILL Photonics, Gräfelfing, Germany**), a 560 nm dichroic mirror (#XF2017; **Omega, Brattleboro, VT, USA**), a 656 long pass emission filter (XF3085; **Omega**) and a CoolSNAP HD camera (**Roper Scientific, Evry Cedex, France**). For each cell, mitochondrial TMRM fluorescence was manually determined in two regions of interest (ROIs) defined in a mitochondria-dense and nucleoplasmic part of the cell and corrected for background using an ROI outside of the cell (**Fig. EV2D**).

Quantification of mitochondrial DNA content **-** Total DNA was isolated using the QIAamp DNA Mini Kit (**Qiagen, Manchester, UK**), according to the manufacturer's guidelines. DNA was eluted (100 µl elution buffer), and concentration was determined by NanoDrop (Labtech International, UK). To avoid dilution bias (**Malik *et al.*, 2011**), 30 µl of template DNA at a concentration of 10 ng/ µl was fragmented by sonication for 10 min at 38 kHz in a bath sonicator (**Pulsatron 55; Kerry Ultrasonics, London, UK**). Real-time qPCR was used to quantify absolute copy number of mtDNA per cell using primer sequences targeting human mtDNA (hMito) and the human nuclear gene beta-2-microglobulin (hB2M) (see: **Thubron *et al.*, 2019** for primer sequences). Each 10 µl reaction consisted of 8 µl Master Mix (5 µl 2x Quantifast SYBR Green Master Mix (**Qiagen**), 500 nM forward and reverse primer, made up to volume with RNAase-free water) and 2 µl total DNA. Samples were loaded onto a 96-well plate in triplicate alongside a standard curve consisting of a serial dilution of 10^8–10^2 copies of primer-specific PCR amplicons. All reactions were performed using the LightCycler 96 Real Time PCR System (**Roche Diagnostics Merck**) and adhering to the MIQE (minimum information for publication of quantitative real-time PCR experiments) guidelines (**Bustin *et al.*, 2009**). Absolute mtDNA copy number was calculated using the standard curve and is presented as a ratio of mitochondrial (hMito) to nuclear (hB2M) targets, representing cellular mtDNA content as described previously (MtN; **Malik *et al.*, 2011; Ajaz *et al.*, 2015**).

Electron microscopy - This approach was adapted from our earlier study (**Koopman *et al.*, 2008a**). Cells were seeded on Corning 35 mm dishes (430166), induced with doxycycline and optionally treated with CAP as described for the TMRM measurements (see above). Cells were fixed for 1 h in 2% glutaraldehyde in 0.1 M sodium cacodylate buffer (CaCo) and post-fixed for 30 min in 1% osmium tetroxide and 1% potassium ferrocyanide in 0.1 M CaCo. After being washed in buffer, cells were dehydrated in an ascending series of aqueous ethanol and were subsequently transferred via a mixture of ethanol and Epon to pure Epon as embedding medium. Sections of 80 nm were cut parallel to the bottom of the dishes, contrasted with 2%

uranyl acetate, counterstained with lead citrate and examined in a JEOL JEM 1400 electron microscope (**JEOL Europe B.V., Nieuw-Vennep, The Netherlands**) operating at 80 kV. Mitochondrial length was determined with Fiji software (https://imagej.net/Fiji) using the Analyse/Measure option and drawing a line transecting the mitochondrion. The number of cristae was manually counted. Next, for each mitochondrion the number of cristae per µm was calculated by dividing the number of cristae by mitochondrial length.

Simulation modelling of mitochondrial FRAP experiments - Our FRAP analysis demonstrates that all AcGFP1 concatemers are highly mobile within the mitochondrial matrix in the absence of chloramphenicol (*i.e.* $F_\infty > 91\%$; **Table 1**). To allow interpretation of T_{mono} in terms of a mitochondrial matrix solvent-dependent solute diffusion constant ($D_{solvent}$) and calculation of mitochondrial matrix solvent viscosity ($\eta_{solvent}$; see below), we developed a particle-based Brownian Dynamics (BD) simulation model (*e.g.* **Erban, 2014; Huber & McCammon, 2019**). Fluorescence correlation spectroscopy (FCS) experiments demonstrated that EYFP in the mitochondrial matrix is not affecting its own diffusion up to a concentration of 10 µM (**Willems *et al.*, 2009**). Therefore, in the BD model we routinely used an FP concentration (C_P) of 10 µM and assumed that FPs move independently. Given the fact that AcGFP1 is an inert monomeric protein (**Bulina *et al.*, 2006; Bell *et al.*, 2007**), with no known binding partners, it was further assumed that AcGFP1 does not bind to the MIM (*i.e.* individual FP molecules display reflections at the MIM). In BD simulations, the three dimensional (3D) position $\mathbf{r}_i$ of the i^{th} particle as a function of time t is integrated over a time step Δt according to:

$$\mathbf{r}_i(t + \Delta t) = \mathbf{r}_i(t) + \sqrt{2D_{solvent}\Delta t}\,\boldsymbol{\theta}_i(t) \qquad \textbf{[Equation-IV]}$$

where the three components to the random vector $\boldsymbol{\theta}_i(t)$ have zero mean, unit standard deviation and are devoid of correlations (Markovian). The diffusion coefficient was varied between 0.5 and 50 $\mu m^2/s$ and the time step was set at $\Delta t = 10^{-5}\ \mu m^2/D_{solvent}$ across all simulations. The mitochondrion was modelled as a cylinder with a radius R_{mito} and a length L_{mito}. (**Appendix Fig. S3A**). These parameters were experimentally determined (**Table 1**) by intensity profile analyses as described previously (see: **Willems *et al.*, 2009** and **Appendix Fig. S2F**). In order to account for diffusion hindrance by mitochondrial cristae (**Ölveczky et al., 1998; Partikian et al., 1998; Dieteren *et al.*, 2011**), we performed EM analysis of mitochondrial ultrastructure (**Fig. 5A** and **Table 1**). Based upon this analysis and information in the literature (**Appelhans *et al.*, 2011; Wilkens *et al.*, 2012; Wolf *et al.*, 2019; Segawa *et al.*, 2020; Hu *et al.*, 2020; Weissert *et al.*, 2021**) it was assumed in the model that: (**1**) mitochondria contained regularly arranged cristae of negligible thickness perpendicular to the longitudinal axis of the mitochondrion, (**2**) the orientations of the cristae alternated, with consecutive cristae blocking - $R_{mito} \leq z \leq -R_{mito} + h$ and $R_{mito} - h \leq z \leq R_{mito}$,, respectively, with h being the length of each crista (**Appendix Fig. S3A**). The presence of cristae increased the effective length of the "channel" that connected the two ends of the mitochondrion thereby increasing FP diffusion length (**Dieteren *et al.*, 2011**). In addition, the presence of cristae reduced the diffusive flow between consecutive mitochondrial sub-compartments. All flat and cylindrical walls were implemented using the appropriate bounce-back rules and it was verified that these rules conserved a uniform density near all surfaces. Simulations were initiated by randomly distributing FP-representing particles throughout the mitochondrial matrix volume. During the bleaching phase of the simulation (lasting 0.1 s; identical to experiments), all particles within the FRAP region (S_{FRAP} = 1.4 µm; identical to experiments) at one end of the cylinder were bleached. In the subsequent recovery simulation, the number of unbleached particles in this region was monitored to compute the FRAP signal. The generated FRAP curves were averaged over ten independent simulations (*e.g.* **Appendix Fig. S3B-C**). These average curves were fitted with the same mono-exponential equation (**[Equation-II]**) as the experimental data to extract T_{mono}. This also allowed calculation of F_m and F_∞ (as explained above). Analysis of the simulated FRAP data demonstrated that each curve ultimately converged to an F_∞ value of 1.0 (*i.e.* 100% fluorescence recovery; equalling F_m and F_∞ values of 1). To compute $D_{solvent}$ from the experimental T_{mono} values, LOG10($D_{solvent}$) was plotted as a function of LOG(T_{mono}) for the simulated FRAP curves and fitted with a straight line (**Fig. 3D** and **Appendix Fig. S3D**):

$$\mathrm{LOG10}(\mathrm{D_{solvent}}) = \mathrm{A} + \mathrm{B} \cdot \mathrm{LOG10}(T_{mono}) \qquad \textbf{[Equation-V]}$$

This yields values for A (intercept) and B (slope), which allows calculation of $D_{solvent}$ by inserting the experimental T_{mono} value.

Calculation of solvent viscosity ($\eta_{solvent}$) from $D_{solvent}$ using the He-Niemeyer equation - This equation is a modified Stokes-Einstein relationship that quantitatively links $D_{solvent}$ and $\eta_{solvent}$ for freely diffusing spherical and cylindrical molecules (**He & Niemeyer, 2003**). We have previously applied this equation in our FRAP analysis of matrix-diffusing AcGFP1 and AcGFP1[2] in HEK293 cells (**Dieteren *et al.*, 2011**):

$$\mathrm{D_{solvent}} = \frac{6.85 \cdot 10^{-8}\mathrm{T}}{\eta_{\mathrm{solvent}} \cdot \sqrt{\mathrm{MW}^{\frac{1}{3}} \cdot \mathrm{R_G}}} \qquad \textbf{[Equation-VI]}$$

With T = temperature (in K; 293 K = 20 °C), $\eta_{solvent}$ = solvent viscosity (in cP; 1 cP = 10^{-3} Pa·s), MW = solute molecular weight (in g/mol), $D_{solvent}$ = solvent-dependent diffusion constant (in cm^2/s; 1.0 cm^2/s = $1.0x10^8$ $\mu m^2/s$), and R_G = radius of gyration (in Angstrom; Å; 1 Å = $1.0x10^{-10}$ m). Here we used **[Equation-VI]** to calculate $\eta_{solvent}$ from $D_{solvent}$ by rewriting as follows:

$$\eta_{\mathrm{solvent}} = \frac{6.85 \cdot 10^{-8}\mathrm{T}}{\mathrm{D_{solvent}} \sqrt{\mathrm{MW}^{\frac{1}{3}} \cdot \mathrm{R_G}}} \qquad \textbf{[Equation-VII]}$$

For calculating $\eta_{solvent}$, the values of T (=293K), MW (determined using the protein sequence; **Appendix Table S1**) and $D_{solvent}$ (from the BD model) are known. This means that R_G needs to be determined for each AcGFP1 concatemer. Assuming that AcGFP1 displays a (minimal) spherical conformation, its R_G value can be calculated from the hydrodynamic radius (R_H) according to (**Dashevskaya *et al.*, 2008**):

$$\mathrm{R_G} = \sqrt{\frac{3}{5}} \cdot \mathrm{R_H} = 0.775 \cdot \mathrm{R_H} \qquad \textbf{[Equation-VIII]}$$

For AcGFP1, R_H = 20Å (**Terry *et al.*, 1995; Arrio-Dupont *et al.*, 2000; Lavalette *et al.*, 2006**) so R_G = 15.5Å, compatible with molecular modelling results for GFP (**Dashevskaya *et al.*, 2008**). Inspection of the GFP crystal structure (**Yang *et al.*, 1996**) predicts an AcGFP1 radius (R) and length (L) of 15Å and 40Å, respectively (**Figure EV1A**). Because AcGFP1[2], AcGFP1[3] and AcGFP1[4] may assume a non-spherical shape in the mitochondrial matrix solvent, **[Equation-VIII]** cannot be applied to determine their R_G value. In principle, AcGFP1[2], AcGFP1[3] and AcGFP1[4] can assume two extreme configurations: "compact" and "extended" (**Figure EV1B-G**). In their extended configuration, we assumed the AcGFP1 concatemer structure to be cylindrical. For a rigid cylinder, the R_G about its centroidal x-axis or y-axis is given by:

$$\mathrm{R_G} = \frac{\sqrt{9 \cdot \mathrm{R}^2 + 3 \cdot \mathrm{L}^2}}{6} \qquad \textbf{[Equation-IX]}$$

In which R is the radius and L is the length of the cylinder. In case of AcGFP1[2], its two AcGFP1 molecules are connected by a 14 AA linker (**Appendix Table S1**). For the compact AcGFP1[2] configuration R = 20Å, L = 60Å and R_G = 20.0 Å (**Table 1** and **Figure EV1B**). When maximally stretched out, this linker has a length of 50.4Å (**Minier & Sigel, 2004**). This means that for the extended AcGFP1[2] configuration R = 15Å, L = 130Å and R_G = 38Å (**Figure EV1C**). Similar calculations were carried out for AcGFP1[3] and AcGFP1[4] (**Table 1**) yielding R_G values of 20Å (AcGFP1[3]-compact), 73Å (AcGFP1[3]-extended), 20Å (AcGFP1[4]-

compact) and 102Å (AcGFP1[4]-extended). Inserting T, $D_{solvent}$, MW and R_G in **[Equation-VII]** was used to calculate $\eta_{solvent}$ for each AcGFP1 concatemer (**Table 1**).

Calculation of solvent viscosity ($\eta_{solvent}$) from $D_{solvent}$ using the Young equation - The Young equation (**Young, 1980**) predicts $\eta_{solvent}$ from $D_{solvent}$ based upon the MW of the solute:

$$D_{solvent} = 8.34 \times 10^{-8} \left(\frac{T}{\eta_{solvent} \cdot MW^{\frac{1}{3}}} \right) \qquad \textbf{[Equation-X]}$$

equalling:

$$\eta_{solvent} = 8.34 \times 10^{-8} \left(\frac{T}{D_{solvent} \cdot MW^{\frac{1}{3}}} \right) \qquad \textbf{[Equation-XI]}$$

With: T = temperature (in K), $\eta_{solvent}$ = solvent viscosity (in cP), MW = solute molecular weight (in g/mol), $D_{solvent}$ = solvent-dependent diffusion constant (in cm^2/s).

Calculation of solvent viscosity ($\eta_{solvent}$) from $D_{solvent}$ using the Tyn-Gusek equation - This approach allows prediction of $\eta_{solvent}$ from $D_{solvent}$ and R_G (**Tyn & Gusek, 1990**):

$$D_{solvent} = 5.78 \times 10^{-8} \left(\frac{T}{\eta_{solvent} \cdot R_G} \right) \qquad \textbf{[Equation-XII]}$$

equalling:

$$\eta_{solvent} = 5.78 \times 10^{-8} \left(\frac{T}{D_{solvent} \cdot R_G} \right) \qquad \textbf{[Equation-XIII]}$$

With T = temperature (in K), $\eta_{solvent}$ = solvent viscosity (in cP), $D_{solvent}$ = solvent-dependent diffusion constant (in cm^2/s), R_G = solute radius of gyration (in Å).

Calculation of solvent viscosity ($\eta_{solvent}$) from $D_{solvent}$ using the Stokes-Einstein equation - The Stokes-Einstein equation describes the diffusion of spherical particles through a liquid (**Einstein, 1905; Sutherland, 1905; von Smoluchowski, 1906**):

$$D_{solvent} = \frac{\kappa_B \cdot T}{6 \cdot \pi \cdot \eta_{solvent} \cdot R_H} \qquad \textbf{[Equation-XIV]}$$

equalling:

$$\eta_{solvent} = \frac{\kappa_B \cdot T}{6 \cdot \pi \cdot D_{solvent} \cdot R_H} \qquad \textbf{[Equation-XV]}$$

With T = temperature (in K), $\eta_{solvent}$ = solvent viscosity (in Pa·s; 1 Pa·s = 10^3 cP), $D_{solvent}$ = solvent-dependent diffusion constant (in m^2/s; 1.0 m^2/s = 1.0×10^{12} $\mu m^2/s$), κ_B = Boltzmann's constant (1.38065×10^{-23} J/K), R_H = solute hydrodynamic radius (in m). For AcGFP1, R_H = 20Å was taken from the literature (**Terry *et al.*, 1995; Arrio-Dupont *et al.*, 2000; Lavalette *et al.*, 2006**). The other AcGFP1 concatemers in their compact and extended configurations (**Figure EV1B-G**) were modelled as prolate ellipsoids (**Perrin, 1936**). In this case their R_H is given by:

$$R_H = \frac{\sqrt{(a^2-b^2)}}{\ln\left(\frac{a+\sqrt{(a^2-b^2)}}{b}\right)}$$ **[Equation-XVI]**

With a = major semi-axis of the ellipse = L/2; b = minor semi-axis of the ellipse = R; L = length of major axis of the ellipsoid (in Å); R = length of minor axis of the ellipsoid (in Å).

2. Appendix Supplementary Results

Chloramphenicol but not doxycycline induces a glycolytic switch - To allow interpretation of the observed CAP effects on FP diffusion in a functional context, we first studied the oxygen consumption rate (OCR) and extracellular acidification rate (ECAR) in HeLa parental cells (**Divakaruni *et al.*, 2022**). The incubation protocols were identical to those used for FP-induced cells ("+DOX" condition: 1 µg/ml; 24 h) and CAP-treatment of FP-induced cells (*i.e.* "+DOX+CAP": 40 µg/ml CAP for 48 h, followed by 40 µg/ml CAP + 1 µg/ml DOX for 24 h). As a control, we also determined the effect of CAP itself ("+CAP": 40 µg/ml for 72 h). After recording basal OCR/ECAR values, various chemicals were added (**Figure EV2A-B**) to inhibit the F_oF_1-ATPAse (oligomycin; OLI), induce mitochondrial uncoupling (FCCP) and inhibit OXPHOS complex I (rotenone; ROT) and complex III (antimycin A; AA). Basal and maximal OCR were slightly increased in the +DOX condition and greatly reduced in the +CAP and +DOX+CAP condition (**Figure EV2C**). Basal ECAR was slightly increased in the +DOX condition and greatly increased in the +CAP and +DOX+CAP condition (**Figure EV2C**). Basal/maximal OCR and basal ECAR values did not significantly differ between the +CAP and +DOX+CAP condition (**Figure EV2C**). Taken together, these results demonstrate that DOX treatment does not inhibit mitochondrial oxygen consumption. In contrast, CAP reduces mitochondrial respiration and increases ECAR, suggesting induction of a glycolytic switch, which was not affected by DOX.

Chloramphenicol increases mitochondrial TMRM fluorescence - Given the central role of the electron transport chain (ETC) in sustaining the mitochondrial membrane potential ($\Delta\psi$), it was next determined whether CAP affected the accumulation of the fluorescent cation TMRM, which can be used as a semi-quantitative readout of $\Delta\psi$ (**Koopman *et al.*, 2008b**). It was found that CAP treatment of HeLa parental cells increased and decreased the mitochondrial and nuclear TMRM fluorescence, respectively (**Figure EV2D**). This suggest that CAP treatment induces $\Delta\psi$ hyperpolarization.

Chloramphenicol and doxycycline do not increase the protein levels of mitochondrial unfolded protein response markers - Evidence in the literature suggests that CAP and DOX can induce the mitochondrial unfolded protein response (UPR^{mt}), which is classically linked to the accumulation of misfolded proteins in the mitochondrial matrix (**Houtkooper *et al.*, 2013; Moullan *et al.*, 2015; Shpilka and Haynes, 2018**). In this way, the observed effects on FP mobility might be due to a CAP- and/or DOX-induced accumulation of unfolded proteins in the mitochondria matrix. UPR^{mt} activation is characterized by upregulation of nuclear genes that encode mitochondrial stress proteins (**Zhao *et al.*, 2002**). The latter include mitochondrial heat shock protein 60 (mtHSP60) and the mitochondrial ATP-dependent Clp protease proteolytic subunit (CLPP). MtHSP60 promotor activity is controlled by the DNA damage-inducible transcript 3 protein (CHOP/CHOP-10/DDIT3) transcription factor. However, CHOP is also involved in the endoplasmic reticulum unfolded protein response (UPR^{ER}) and therefore not UPR^{mt} specific (**Zhao *et al.*, 2002**). In addition, UPR^{mt} activation was previously linked to increased protein levels of the mitochondrial Lon Peptidase 1 (LONP1; **Xu *et al.*, 2016**) and reduced function of mitochondrial heat shock protein 70 (mtHSP70/mortalin; **Burbulla *et al.*, 2014**). Analysis of HeLa parental cells (**Figure EV2E**) and FP-expressing cells (**Figure EV3A**) revealed no changes in the above protein levels upon treatment with DOX, CAP or DOX+CAP. For statistical analysis we reasoned that if DOX and/or CAP would affect the

level of the UPR^{mt}-linked proteins, the effect on the expression pattern of these proteins should be similar in all five HeLa cell lines (*i.e.* parental and four FP-expressing). This analysis revealed no UPR^{mt}-characteristic changes in the expression pattern of LONP1, mtHSP70, mtHSP70, CLPP and CHOP (**Figure EV3B**). These results suggest that UPR^{mt} activation is not responsible for the CAP-induced increase in $D_{solvent}$.

Chloramphenicol does not alter mitochondrial DNA copy number and the level of key mitochondrial fission and fusion proteins - Within cells, mtDNA is associated in nucleoprotein complexes ("nucleoids") and evidence in *E. coli* demonstrated that nucleoids undergo changes in shape and compaction upon CAP treatment (**Van Helvoort *et al.*, 1996**). Mitochondrial cristae structure also appears to compartmentalize nucleoids thereby preventing their free matrix diffusion (**Nicholls & Gustafsson, 2018**). Substantial nucleoid aggregation was observed upon loss of specific isoforms of the key MIM fusion protein Optic atrophy protein 1 (OPA1), which controls cristae structure and might be involved in mtDNA to MIM attachment (**Elachouri *et al.*, 2011**). Moreover, CAP prevented stress-induced OPA1 processing during dysfunction of the mitochondrial AAA protease AFG3L2 (**Richter *et al.*, 2019**). In this way, alterations in mtDNA and/or OPA1 level/processing might affect solute diffusion in CAP-treated cells. Here we observed that CAP treatment did not affect mtDNA copy number in HeLa parental cells (**Figure EV2F**). Similarly, the level of OPA1 and two other key MOM fission/fusion proteins (DRP1, MFN2) was not affected by CAP (**Figure EV2G**). This demonstrates that the observed CAP-induced increase in $D_{solvent}$ is not linked to alterations in the levels of mtDNA, OPA1, DRP1 or MFN2.

Predicted level of macromolecules and volume exclusion in the absence and presence of CAP - To obtain an semiquantitative estimate of the degree of macromolecular crowding within the mitochondrial matrix solvent of HeLa cells, we used human serum albumin (HSA) as a theoretical crowding agent. The MW of hydrated HSA equals 91.675 kDa (*i.e.* 91.675 $x10^3$ g/mol). Structurally, hydrated HSA is a prolate ellipsoid with semi-diameters: a = 8.2 nm and b = 2.1 nm. Computing the volume of this ellipsoid ($V_{ellipsoid,prolate} = (4/3)\cdot\pi\cdot b^2\cdot a$) yields a HSA molecular volume of 151 nm^3 (*i.e.* $1.51\cdot10^{-22}$ l). The total volume of the mitochondrial matrix (V_{mito}) equals $\approx 8.0\cdot10^{-16}$ l (**Table 1**). This means that $\approx 5.28\cdot10^6$ HSA molecules will fit in the mitochondrial matrix.

- *In the absence of CAP*, the matrix solvent viscosity ($\eta_{solvent}$) was maximally 4.57 cP (**Fig. 4C**). At 20° C this viscosity value was reached at HSA concentrations of $\approx$ 198 kg/m^3 in distilled water (**Monkos, 2004**). This concentration equals $198/91.675\cdot10^3 = 2.16\cdot10^{-3}$ mol and $2.16\cdot10^{-3}$ x $6.0221\cdot10^{23}$ (N_A) = $1.30\cdot10^{21}$ molecules/l. With a V_{mito} of $8.0\cdot10^{-16}$ l this equals a total number of $1.30\cdot10^{21}$ x $8.0\cdot10^{-16}$ = $1.04\cdot10^6$ molecules. These molecules occupy a volume fraction of $1.04\cdot10^6$ / $5.28\cdot10^6$ = 19.7% of the total mitochondrial matrix volume.

In CAP-treated cells $\eta_{solvent}$ increased to a maximal value of 37.5 cP (**Fig. 5G**), being equivalent to a HSA concentration of $\approx$ 328 kg/m^3 (**Monkos, 2004**). These concentrations are equivalent to $1.72\cdot10^6$ molecules in the mitochondrial matrix, which suggests that in the presence of CAP 32.7% of the total mitochondrial matrix volume is occupied by proteins. The HSA-occupied volume is not accessible by other molecules, a phenomenon described as the "excluded volume" effect (**Minton, 1981**). In this sense, the predicted HSA volume fractions in the absence and presence of CAP agree with those reported in *E. Coli* being between 5% and 40% of the cell volume (**Akabayov *et al.*, 2013**).

3. Appendix Supplementary Figures

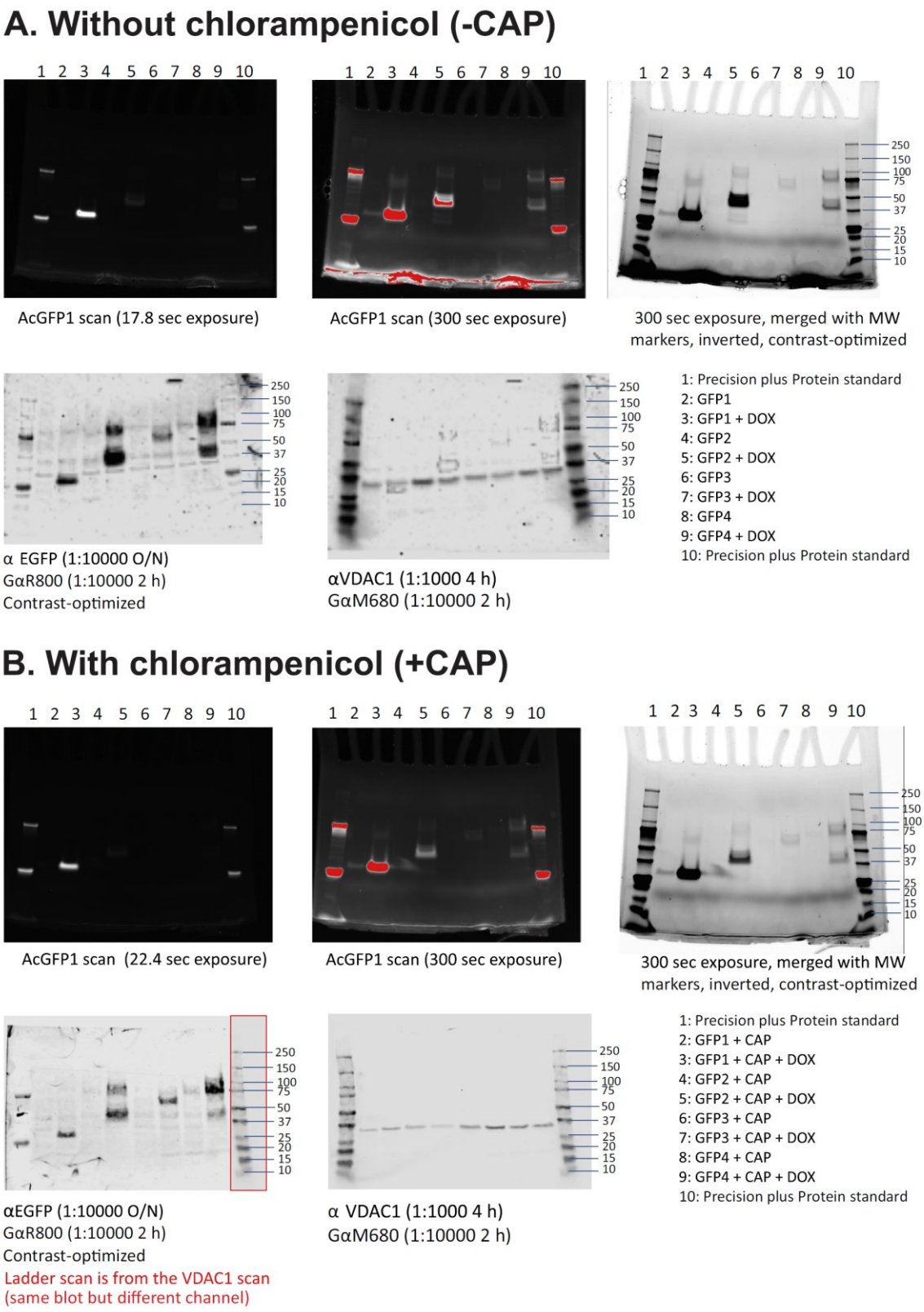

Appendix Figure S1: Original in-gel fluorescence scans and Western blots. The data in panel A was used to create **Fig. 2B**. The data in panel B is virtually identical to panel A, but was obtained for cells cultured in the presence of chloramphenicol (CAP).

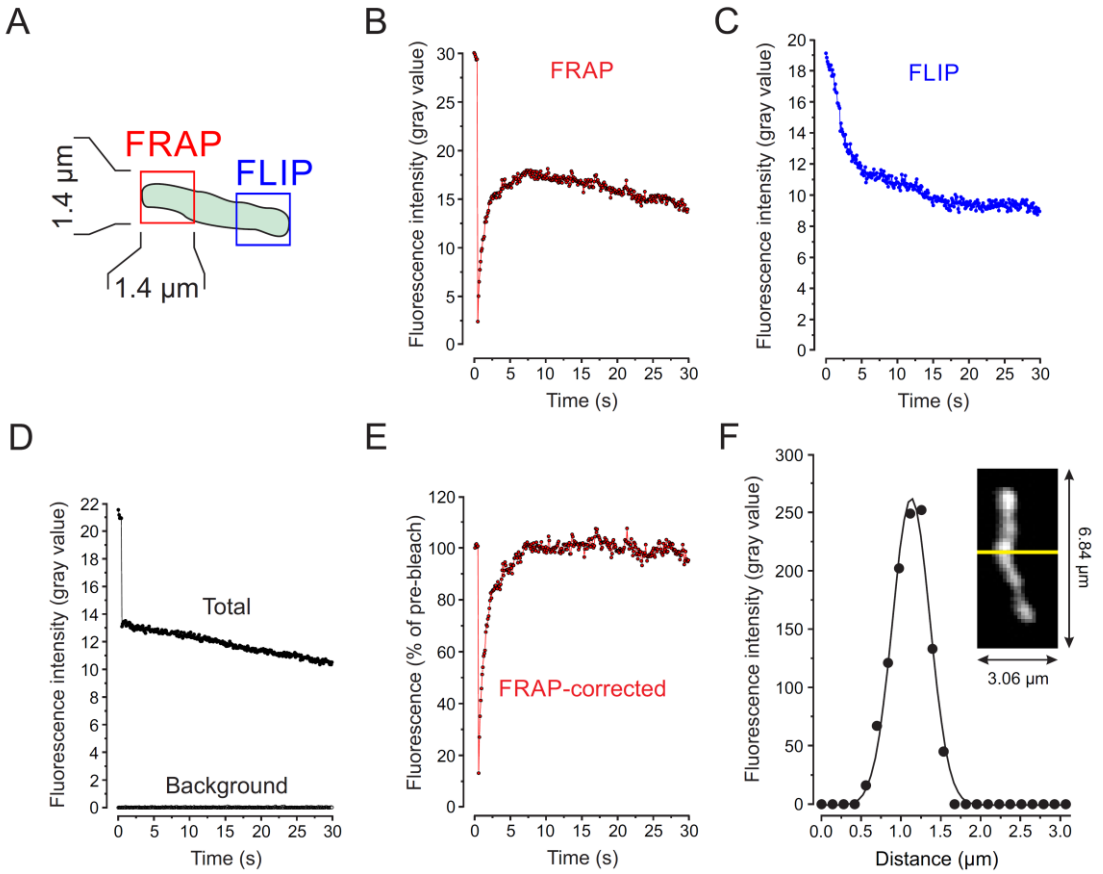

Appendix Figure S2: Analysis of mitochondrial fluorescence recovery after photobleaching (FRAP) experiments and quantification of mitochondrial radius (R_{mito}) and length (L_{mito}). In this typical example, a FRAP recording from a mitochondrion in an mitochondria-targeted AcGFP1-expressing HeLa cell is presented. (**A**) Geometry of the FRAP experiment. Two regions of interest (ROIs) were placed on both ends of the mitochondrion. AcGFP1 photobleaching was performed using a 1.4x1.4 µm FRAP region. Only single mitochondria that were fully located within the focal plane were used for analysis (confirmed by an axial scan). Only mitochondria in which FRAP was paralleled by fluorescence loss in photobleaching (FLIP) in a part distal to the FRAP region were considered to possess a continuous mitochondrial matrix and included in the analysis. (**B**) Time course of the fluorescence signal in the FRAP region. First, a pre-bleach fluorescence level was recorded, after which AcGFP1 was photobleached (fast signal drop) and fluorescence recovery (slower increase) was measured. (**C**) Time course of the fluorescence signal in the FLIP region. (**D**) Fluorescence signal in a ROI placed just outside the mitochondrion ("Background") and a rotated rectangular ROI around the complete mitochondrion ("Total"). (**E**) Time course of the corrected FRAP curve. In our experiments the size of the FRAP region is relatively large in comparison to the total size of the mitochondrion. Therefore, the experimental FRAP curve in panel B was corrected using the information in panel C and D using **[Equation-I]**. This also corrects for photobleaching during image acquisition (visible in panel D; total signal). (**F**) Determination of mitochondrial diameter (D_{mito}) from confocal microscopy fluorescence images (**Willems *et al.*, 2009**). Mitochondrial diameter D_{mito} (equalling $2 \cdot R_{mito}$) was assessed by quantifying the intensity of a 1 pixel wide profile perpendicular to the long axis of the mitochondrial filament (yellow line; image was linearly contrast stretched for visualization purposes). The width (w) of this profile at its half-maximal height is determined by fitting a Gaussian curve: $y=y_0+\{A/[w \cdot \sqrt{(\pi/2)}]\} \cdot EXP\{-2 \cdot [(x-x_c)^2/w^2]\}$. For the given example this yielded $\underline{w}$=0.469 µm (*i.e.* R_{mito}=0.248 µm) and R^2=0.988. A similar strategy was used to determine mitochondrial length (L_{mito}) by analysing the intensity profile along the length axis of the mitochondrion.

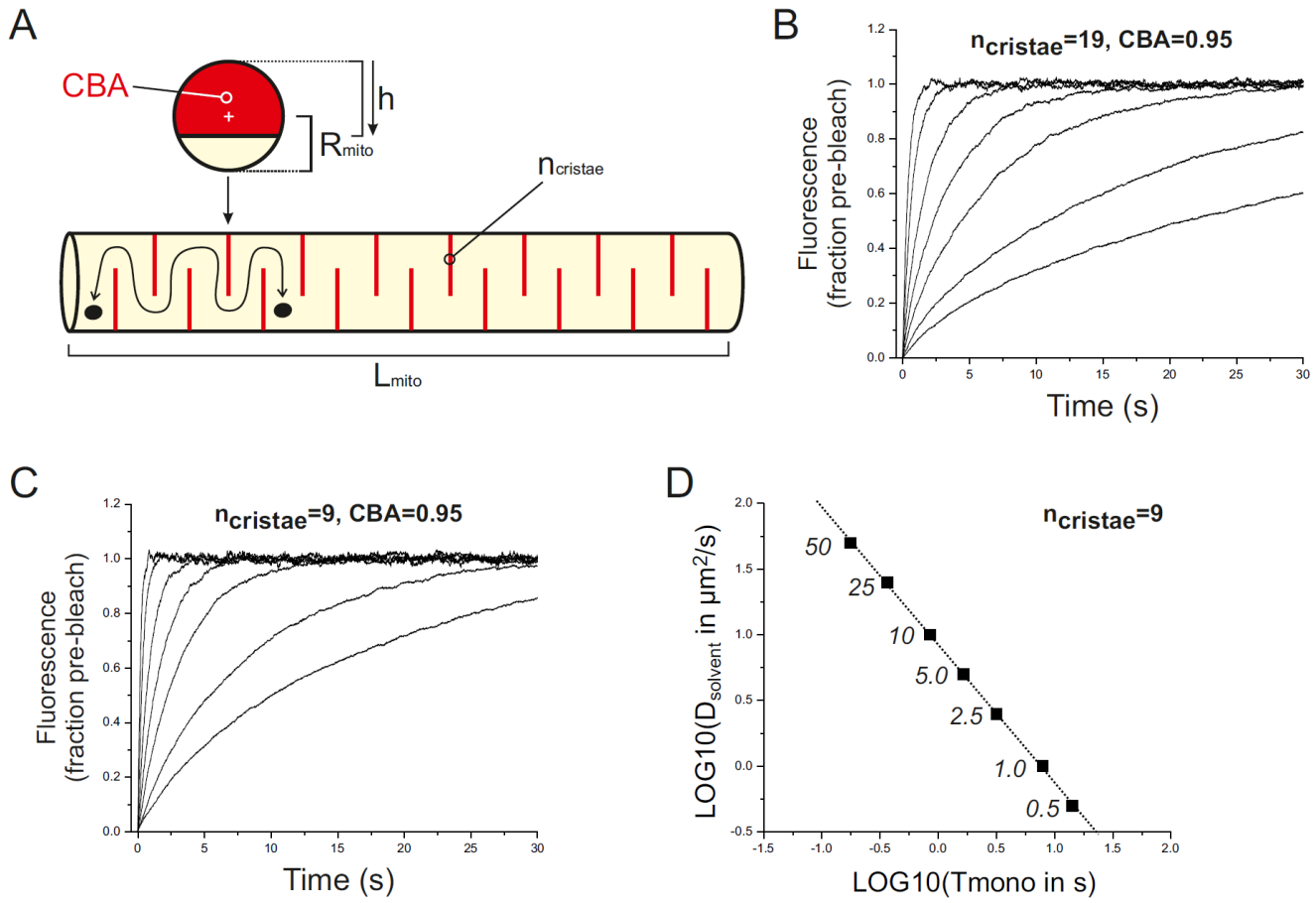

Appendix Figure S3: Synthetic FRAP data generated by the BD model. (**A**) Geometry of the BD model. See **Appendix** and **Results** for details. (**B**) Simulated FRAP curves for different values of the solvent-dependent diffusion constant ($D_{solvent}$; see panel D for exact values in $\mu m^2/s$). The number of cristae/mito ($n_{cristae}$) equalled 19. The cristae-blocked area (CBA) equalled 0.95. (**C**) Same as panel B but now for $n_{cristae}$ = 9 and CBA=0.95. (**D**) Linear relationship **[Equation-VI]** between the FRAP recovery time constant (T_{mono}) and the $D_{solvent}$ value (logarithmic scale) for the data in panel C (R=-0.999, p<0.0001; A(intercept)=0.923±0.00569(SE); B(slope)= -1.05±0.00841 (SE)).

A

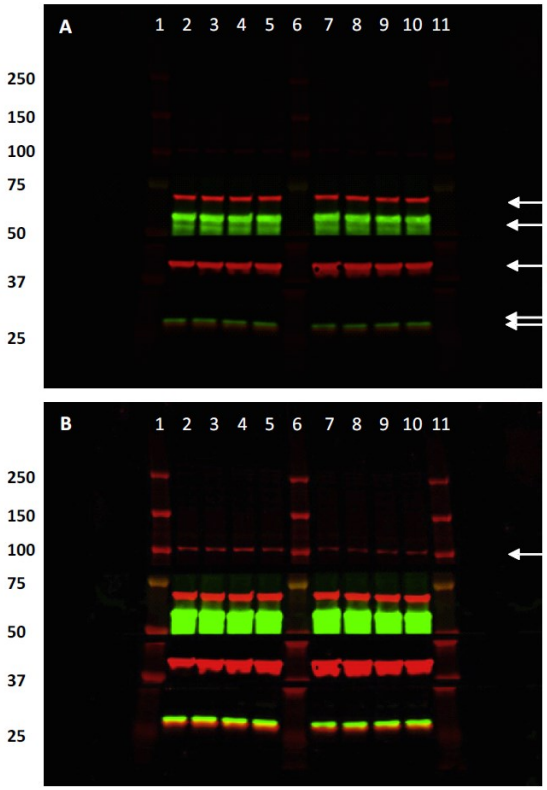

Legend:

1. Precision Plus Protein standards Dual color
2. HeLa T-Rex Flp-In cox8-AcGFP1-CAP/-DOX
3. HeLa T-Rex Flp-In cox8-AcGFP1-CAP/+DOX
4. HeLa T-Rex Flp-In cox8-AcGFP1 +CAP/-DOX
5. HeLa T-Rex Flp-In cox8-AcGFP1 +CAP/+DOX
6. Precision Plus Protein standards Dual color
7. HeLa T-Rex Flp-In cox8-AcGFP2-CAP/-DOX
8. HeLa T-Rex Flp-In cox8-AcGFP2-CAP/+DOX
9. HeLa T-Rex Flp-In cox8-AcGFP2 +CAP/-DOX
10. HeLa T-Rex Flp-In cox8-AcGFP2 +CAP/+DOX
11. Precision Plus Protein standards Dual color

- CAP treatment: 72h (40 µg/ml)
- DOX induction: 24h (1 µg/ml)
- Loaded: 20 µg total protein/lane
- 4-15% SDS-PAGE

- LONP1: 106 kDa
- mtHSP70: 70 kDa
- mtHSP60: 60 kDa
- β-actin: 42 kDa
- CLPP: 30 kDa
- CHOP: 29 kDa

- A = Auto scan
- B = Enhanced

B

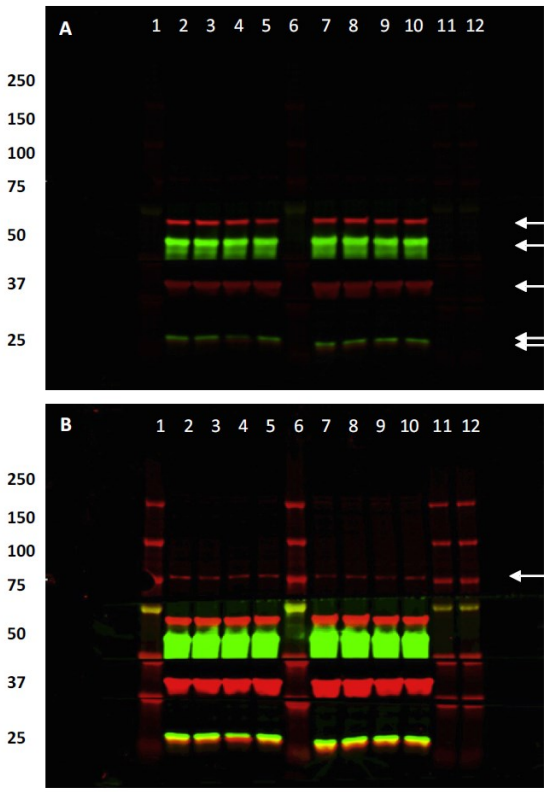

Legend:

1. Precision Plus Protein standards Dual color
2. HeLa T-Rex Flp-In cox8-AcGFP3-CAP/-DOX
3. HeLa T-Rex Flp-In cox8-AcGFP3-CAP/+DOX
4. HeLa T-Rex Flp-In cox8-AcGFP3 +CAP/-DOX
5. HeLa T-Rex Flp-In cox8-AcGFP3 +CAP/+DOX
6. Precision Plus Protein standards Dual color
7. HeLa T-Rex Flp-In cox8-AcGFP4-CAP/-DOX
8. HeLa T-Rex Flp-In cox8-AcGFP4-CAP/+DOX
9. HeLa T-Rex Flp-In cox8-AcGFP4 +CAP/-DOX
10. HeLa T-Rex Flp-In cox8-AcGFP4 +CAP/+DOX
11. Precision Plus Protein standards Dual color
12. Precision Plus Protein standards Dual color

- CAP treatment: 72h (40 µg/ml)
- DOX induction: 24h (1 µg/ml)
- Loaded: 20 µg total protein/lane
- 4-15% SDS-PAGE

- LONP1: 106 kDa
- mtHSP70: 70 kDa
- mtHSP60: 60 kDa
- β-actin: 42 kDa
- CLPP: 30 kDa
- CHOP: 29 kDa

- A = Auto scan
- B = Enhanced

Appendix Figure S4: Original blots for analysis of UPR^{mt} proteins in FP-expressing cells.

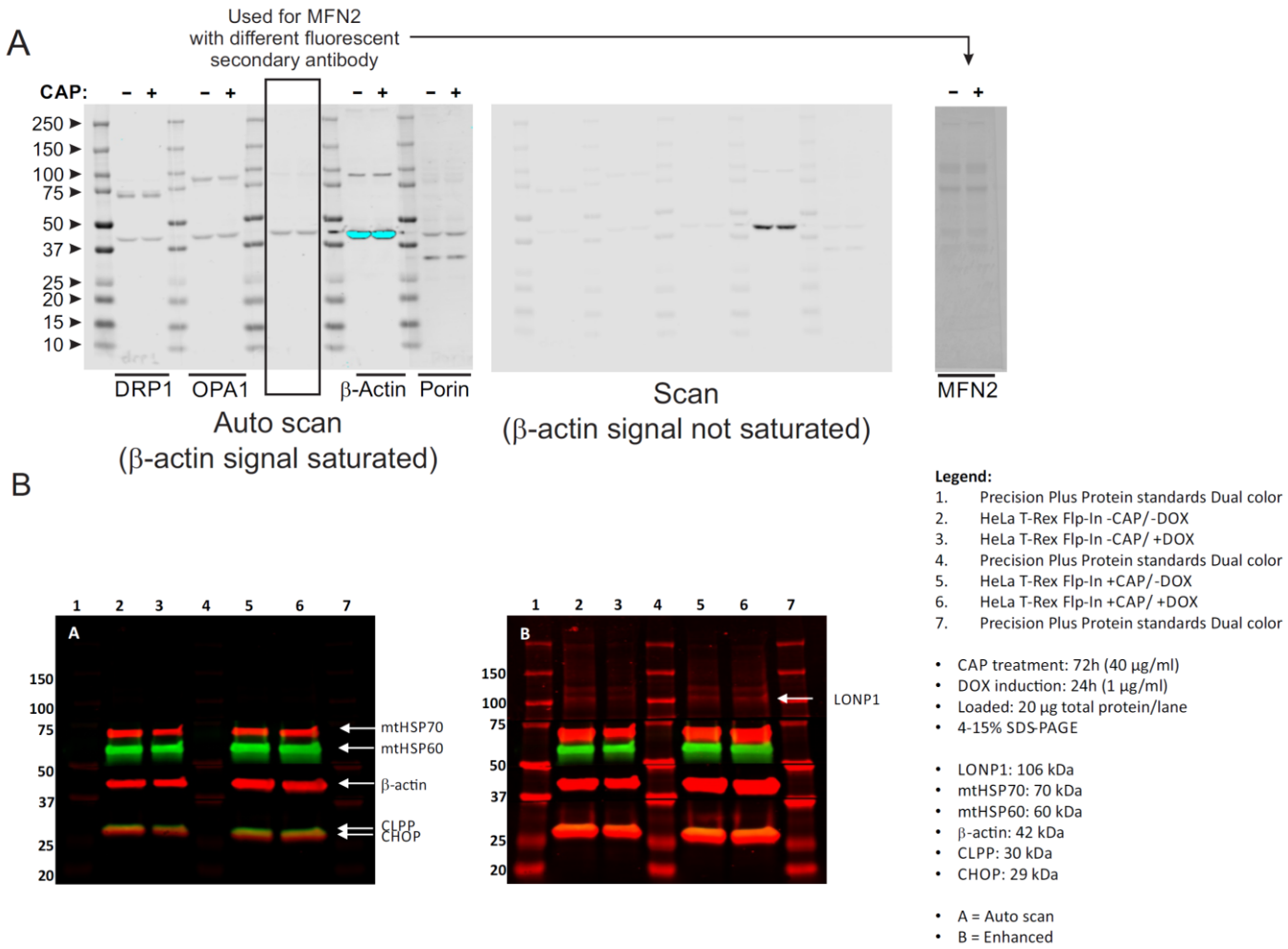

Appendix Figure S5: Original blots for analysis of fission/fusion (panel A) and UPR^{mt} proteins (panel B) in HeLa parental cells.

4. Appendix Supplementary Tables

Appendix Supplementary Table S1: Protein sequences, MW and dimensions of the AcGFP1 concatemers

Sequence	MW and dimensions
Cox8-AcGFP1 MSVLTPLLLRGLTGSARRLPVPRAKIHSLPPHPAFLYKVVDDPPVMVSKGAELFTGIVPILI ELNGDVNGHKFSVSGEGEGDATYGKLTLKFICTTGKLPVPWPTLVTTLSYGVQCFSRYPD HMKQHDFFKSAMPEGYIQERTIFFEDDGNYKSRAEVKFEGDTLVNRIELTGTDFKEDGNI LGNKMEYNYNAHNVYIMTDKAKNGIKVNFKIRHNIEDGSVQLADHYQQNTPIGDGPVLL PDNHYLSTQSALSKDPNEKRDHMIYFGFVTAAAITHGMDELYK	MTS = 2.703 kDa Linker = 2.241 kDa AcGFP1 = 26.874 kDa **Total protein (+MTS) = 31.818 kDa** **Total protein (-MTS) = 29.115 kDa**
Cox8-AcGFP1[2] MSVLTPLLLRGLTGSARRLPVPRAKIHSLPPHPAFLYKVVDDPPVMVSKGAELFTGIVPILI ELNGDVNGHKFSVSGEGEGDATYGKLTLKFICTTGKLPVPWPTLVTTLSYGVQCFSRYPD HMKQHDFFKSAMPEGYIQERTIFFEDDGNYKSRAEVKFEGDTLVNRIELTGTDFKEDGNI LGNKMEYNYNAHNVYIMTDKAKNGIKVNFKIRHNIEDGSVQLADHYQQNTPIGDGPVLL PDNHYLSTQSALSKDPNEKRDHMIYFGFVTAAAITHGMDELYKHPAFLYKVVDDPPVM VSKGAELFTGIVPILIELNGDVNGHKFSVSGEGEGDATYGKLTLKFICTTGKLPVPWPTLV TTLSYGVQCFSRYPDHMKQHDFFKSAMPEGYIQERTIFFEDDGNYKSRAEVKFEGDTLV NRIELTGTDFKEDGNILGNKMEYNYNAHNVYIMTDKAKNGIKVNFKIRHNIEDGSVQLA DHYQQNTPIGDGPVLLPDNHYLSTQSALSKDPNEKRDHMIYFGFVTAAAITHGMDELYK	MTS = 2.703 kDa Linker = 2.241 kDa AcGFP1 = 26.874 kDa Linker = 14AA = 50.4 Å = 1.597 kDa AcGFP1 = 26.874 kDa **Total protein (+MTS) = 60.289 kDa** **Total protein (-MTS) = 57.586 kDa**
Cox8-AcGFP1[3] MSVLTPLLLRGLTGSARRLPVPRAKIHSLPPHPAFLYKVVDDPPVSIKLLAMVSKGAELFT GIVPILIELNGDVNGHKFSVSGEGEGDATYGKLTLKFICTTGKLPVPWPTLVTTLSYGVQC FSRYPDHMKQHDFFKSAMPEGYIQERTIFFEDDGNYKSRAEVKFEGDTLVNRIELTGTDF KEDGNILGNKMEYNYNAHNVYIMTDKAKNGIKVNFKIRHNIEDGSVQLADHYQQNTPIG DGPVLLPDNHYLSTQSALSKDPNEKRDHMIYFGFVTAAAITHGMDELYKDIPPHPAFLYK VVDDPPVMVSKGAELFTGIVPILIELNGDVNGHKFSVSGEGEGDATYGKLTLKFICTTGK LPVPWPTLVTTLSYGVQCFSRYPDHMKQHDFFKSAMPEGYIQERTIFFEDDGNYKSRAEV KFEGDTLVNRIELTGTDFKEDGNILGNKMEYNYNAHNVYIMTDKAKNGIKVNFKIRHNIE DGSVQLADHYQQNTPIGDGPVLLPDNHYLSTQSALSKDPNEKRDHMIYFGFVTAAAITH GMDELYKHPAFLYKVVDDPPVSTCIPVMVSKGAELFTGIVPILIELNGDVNGHKFSVSGE GEGDATYGKLTLKFICTTGKLPVPWPTLVTTLSYGVQCFSRYPDHMKQHDFFKSAMPEG YIQERTIFFEDDGNYKSRAEVKFEGDTLVNRIELTGTDFKEDGNILGNKMEYNYNAHNVY IMTDKAKNGIKVNFKIRHNIEDGSVQLADHYQQNTPIGDGPVLLPDNHYLSTQSALSKDP NEKRDHMIYFGFVTAAAITHGMDELYK	MTS = 2.703 kDa Linker = 2.867 kDa AcGFP1 = 26.874 kDa Linker = 18AA = 64.8 Å = 2.019 kDa AcGFP1 = 26.874 kDa Linker = 20AA = 72.0 Å = 2.197 kDa AcGFP1 = 26.874 kDa **Total protein (+MTS) = 90.408 kDa** **Total protein (-MTS) = 87.705 kDa**
Cox8[2]-AcGFP1[4] MSVLTPLLLRGLTGSARRLPVPRAKIHSLGDPMSVLTPLLLRGLTGSARRLPVPRAKIHSL PPEGDLKPVMVSKGAELFTGIVPILIELNGDVNGHKFSVSGEGEGDATYGKLTLKFICTTG KLPVPWPTLVTTLSYGVQCFSRYPDHMKQHDFFKSAMPEGYIQERTIFFEDDGNYKSRAE VKFEGDTLVNRIELTGTDFKEDGNILGNKMEYNYNAHNVYIMTDKAKNGIKVNFKIRHN IEDGSVQLADHYQQNTPIGDGPVLLPDNHYLSTQSALSKDPNEKRDHMIYFGFVTAAAIT HGMDELYKHPAFLYKVVDDPPVSIKLLAMVSKGAELFTGIVPILIELNGDVNGHKFSVSG EGEGDATYGKLTLKFICTTGKLPVPWPTLVTTLSYGVQCFSRYPDHMKQHDFFKSAMPE GYIQERTIFFEDDGNYKSRAEVKFEGDTLVNRIELTGTDFKEDGNILGNKMEYNYNAHNV YIMTDKAKNGIKVNFKIRHNIEDGSVQLADHYQQNTPIGDGPVLLPDNHYLSTQSALSKD PNEKRDHMIYFGFVTAAAITHGMDELYKDIPPHPAFLYKVVDDPPVMVSKGAELFTGIVP ILIELNGDVNGHKFSVSGEGEGDATYGKLTLKFICTTGKLPVPWPTLVTTLSYGVQCFSRY PDHMKQHDFFKSAMPEGYIQERTIFFEDDGNYKSRAEVKFEGDTLVNRIELTGTDFKEDG NILGNKMEYNYNAHNVYIMTDKAKNGIKVNFKIRHNIEDGSVQLADHYQQNTPIGDGPV LLPDNHYLSTQSALSKDPNEKRDHMIYFGFVTAAAITHGMDELYKHPAFLYKVVDDPPV STCIPVMVSKGAELFTGIVPILIELNGDVNGHKFSVSGEGEGDATYGKLTLKFICTTGKLP VPWPTLVTTLSYGVQCFSRYPDHMKQHDFFKSAMPEGYIQERTIFFEDDGNYKSRAEVK FEGDTLVNRIELTGTDFKEDGNILGNKMEYNYNAHNVYIMTDKAKNGIKVNFKIRHNIED GSVQLADHYQQNTPIGDGPVLLPDNHYLSTQSALSKDPNEKRDHMIYFGFVTAAAITHG MDELYK	MTS = 2.703 kDa Linker = 0.738 kDa MTS = 2.703 kDa Linker = 1.401 kDa AcGFP1 = 26.874 kDa Linker = 20AA = 72.0 Å = 2.223 kDa AcGFP1 = 26.874 kDa Linker = 18AA = 64.8 Å = 2.019 kDa AcGFP1 = 26.874 kDa Linker = 20AA = 72.0 Å = 2.198 kDa AcGFP1 = 26.874 kDa **Total protein (+MTS-linker-MTS) = 121.481 kDa** **Total protein (-MTS-linker-MTS) = 115.337 kDa**

Remarks: Mitochondrial Target Sequence (MTS), the 25-residue Cox8 sequence (**Rizzutto et al., J. Biol. Chem., 1989**). Linker sequences . Linker sequences. AcGFP1 sequence (monomeric *Aequorea coerulescens* Green Fluorescent Protein). The linkers highlighted in black were not considered for geometry calculations of the proteins. Molecular weight was calculated directly from the protein sequence using the pI/Mw tool (web.expasy.org/compute_pi).One (1) Dalton (Da) equals 1 g/mol.

Appendix Supplementary Table S2: Experimental $D_{solvent}$ values in aqueous solution and in the cell

Protein/molecule	MW (kDa)	LOG10 (MW)	$D_{solvent}$ (µm²/s)	LOG10 ($D_{solvent}$)	Reference
GLOBULAR OR SPHERICAL CONFORMATION IN AQUEOUS SOLUTION Fitting results of LOG(MW) *vs.* LOG($D_{solvent}$): **Y=A+B·X:** R=-0.986; P<0.0001; A=2.45±0.0154(SE); B=-0.360±0.00525(SE)					
Insulin	12	1.079	147.0	2.167	**Gribbon *et al.*, 1998**
Cytochrome-*c*	13	1.126	114.0	2.057	**Young *et al.*, 1980**
Ribonuclease	13	1.102	131.0	2.117	**Tyn & Gusek, 1990**
Alpha-lactalbumin	13	1.124	106.0	2.025	**Tyn & Gusek, 1990**
Ribonuclease	14	1.137	117.0	2.068	**Tyn & Gusek, 1990**
Lysozyme	14	1.144	112.0	2.049	**Tyn & Gusek, 1990**
Myoglobin	16	1.204	113.0	2.053	**Tyn & Gusek, 1990**
Ribonuclease	17	1.230	102.0	2.009	**Tyn & Gusek, 1990**
Myokinase	21	1.322	160.0	2.204	**Arrio-Dupont et al., 2000**
Alpha-chymotrypsin (monomer)	21	1.328	102.0	2.009	**Young *et al.*, 1980**
Alpha-chymotrypsinogen	38	1.580	79.0	1.898	**He & Niemeyer, 2003**
Gamma-chymotrypsin	23	1.366	95.0	1.978	**Tyn & Gusek, 1990**
Chymotrypsin A	18	1.243	102.0	2.009	**Tyn & Gusek, 1990**
SBTI	22	1.334	88.0	1.944	**Gribbon *et al.*, 1998**
Ribosome 4S	23	1.365	75.8	1.880	**Tyn & Gusek, 1990**
Beta-casein	24	1.382	60.5	1.782	**Tyn & Gusek, 1990**
Riboflavin-binding protein	33	1.512	74.0	1.869	**Tyn & Gusek, 1990**
Pepsin	33	1.515	87.0	1.940	**Tyn & Gusek, 1990**
Beta-lactoglobulin	35	1.549	78.0	1.892	**Tyn & Gusek, 1990**
Ovalbumin	44	1.643	77.6	1.890	**Tyn & Gusek, 1990**
Phosphoglucomutase	60	1.778	63.8	1.805	**Arrio-Dupont *et al.*, 2000**
Phosphoglycerate kinase	47	1.670	63.8	1.805	**Tyn & Gusek, 1990**
Hemoglobin	63	1.799	69.0	1.839	**Tyn & Gusek, 1990**
Hemoglobin - earthworm	3700	3.568	12.0	1.079	**Papadopoulos *et al.*, 2000**
Bovine serum albumin	65	1.816	61.5	1.789	**Tyn & Gusek, 1990**
Beta-enolase	90	1.954	56.0	1.748	**Arrio-Dupont *et al.*, 2000**
Alpha-amylase	97	1.986	57.2	1.757	**Young *et al.*, 1980**
Citrate synthase	98	1.991	58.0	1.763	**Durchslag & Zipper, 1997**
Hexokinase	99	1.996	60.0	1.778	**Tyn & Gusek, 1990**
Glyceraldehyde-3-phosphate dehydrogenase	141	2.149	50.0	1.699	**Tyn & Gusek, 1990**

Lysine-trna ligase	138	2.140	43.0	1.633	**Tyn & Gusek, 1990**
Lactate dehydrogenase	138	2.141	51.0	1.708	**Tyn & Gusek, 1990**
Phosphofructokinase	142	2.152	53.0	1.724	**Tyn & Gusek, 1990**
Phosphofructokinase	160	2.204	42.0	1.623	**Tyn & Gusek, 1990**
IgG	160	2.204	40.5	1.607	**Arrio-Dupont *et al.*, 2000**
Phosphofructokinase	320	2.505	32.2	1.508	**Tyn & Gusek, 1990**
Beta-lactoglobulin A	147	2.167	42.0	1.623	**Tyn & Gusek, 1990**
Gamma-globulin	153	2.185	40.0	1.602	**Tyn & Gusek, 1990**
Gamma-globulin	162	2.210	37.0	1.568	**Tyn & Gusek, 1990**
Glycogen-phosphorylase	163	2.212	42.0	1.623	**Tyn & Gusek, 1990**
Glycogen-phosphorylase	185	2.267	41.2	1.615	**Tyn & Gusek, 1990**
Malate synthase	170	2.230	45.0	1.653	**Tyn & Gusek, 1990**
Malate synthase	187	2.272	45.0	1.653	**Tyn & Gusek, 1990**
Methionyl-tRNA synthetase	173	2.238	35.0	1.544	**Tyn & Gusek, 1990**
Pyruvate kinase	191	2.281	42.0	1.623	**Tyn & Gusek, 1990**
Catalase	225	2.352	41.0	1.613	**Tyn & Gusek, 1990**
Catalase	232	2.365	41.0	1.613	**Tyn & Gusek, 1990**
Catalase	248	2.394	43.0	1.633	**Papadopoulos *et al.*, 2000**
Catalase	250	2.398	45.0	1.653	**Tyn & Gusek, 1990**
Porphobilinogen synthase	270	2.431	42.0	1.623	**Tyn & Gusek, 1990**
Porphobilinogen synthase	240	2.380	42.0	1.623	**Tyn & Gusek, 1990**
Glutamate dehydrogenase	270	2.431	35.0	1.544	**Tyn & Gusek, 1990**
Glutamate dehydrogenase	312	2.494	35.0	1.544	**Tyn & Gusek, 1990**
Glutamate dehydrogenase	343	2.535	35.0	1.544	**Tyn & Gusek, 1990**
Edestin	310	2.491	39.3	1.594	**Tyn & Gusek, 1990**
Edestin	324	2.511	31.7	1.501	**Tyn & Gusek, 1990**
Adenovirus_Type_2_hexon	323	2.509	35.6	1.551	**Tyn & Gusek, 1990**
Adenovirus_Type_2_hexon	355	2.550	33.2	1.521	**Tyn & Gusek, 1990**
Phosphofructokinase	330	2.519	36.0	1.556	**Tyn & Gusek, 1990**
Phosphofructokinase	340	2.531	32.2	1.508	**Tyn & Gusek, 1990**
DNA-dependent_RNA+polymerase	360	2.556	33.0	1.519	**Tyn & Gusek, 1990**
Glycogen phosphorylase	370	2.568	33.0	1.519	**Tyn & Gusek, 1990**
Cytochrome c1	371	2.569	33.1	1.520	**Young *et al.*, 1980**
Ferritin	450	2.653	38.0	1.580	**Papadopoulos *et al.*, 2000**
Apoferritin	441	2.644	36.1	1.558	**Tyn & Gusek, 1990**
Apoferritin	460	2.663	36.1	1.558	**Tyn & Gusek, 1990**

Apoferritin	467	2.669	36.1	1.558	**Tyn & Gusek, 1990**
Fibronectin	510	2.708	22.7	1.356	**Durchslag & Zipper, 1997**
Beta-galactosidase	540	2.732	30.0	1.477	**Arrio-Dupont *et al.*, 2000**
Thyroglobulin	630	2.799	26.5	1.423	**Tyn & Gusek, 1990**
Thyroglobulin	650	2.813	26.5	1.423	**Tyn & Gusek, 1990**
Thyroglobulin	660	2.820	26.1	1.417	**Tyn & Gusek, 1990**
Ribosome S30	700	2.845	29.5	1.470	**Tyn & Gusek, 1990**
Alpha-crystallin	770	2.886	23.0	1.362	**Tyn & Gusek, 1990**
Alpha-crystallin	840	2.924	23.0	1.362	**Tyn & Gusek, 1990**
Alpha-crystallin	960	2.982	20.0	1.301	**Tyn & Gusek, 1990**
Alpha2-macroglobulin	820	2.914	24.1	1.382	**Tyn & Gusek, 1990**
Alpha2-macroglobulin	985	2.993	24.1	1.382	**Tyn & Gusek, 1990**
Haemocyanin	854	2.931	26.9	1.430	**Tyn & Gusek, 1990**
Ribosome S30	870	2.940	29.5	1.470	**Tyn & Gusek, 1990**
Ribosome S30	900	2.954	29.5	1.470	**Tyn & Gusek, 1990**
Beta-casein	1200	3.079	14.0	1.146	**Tyn & Gusek, 1990**
Ribosome S30	1000	3.000	29.5	1.470	**Tyn & Gusek, 1990**
Ribosome S50	1500	3.176	19.1	1.281	**Tyn & Gusek, 1990**
Ribosome S50	1550	3.190	19.1	1.281	**Tyn & Gusek, 1990**
Ribosome S50	1580	3.199	19.1	1.281	**Tyn & Gusek, 1990**
Ribosome S50	1800	3.255	19.1	1.281	**Tyn & Gusek, 1990**
Ribosome S70	3000	3.477	18.3	1.262	**Tyn & Gusek, 1990**
Fatty-acid synthase	2200	3.342	17.8	1.250	**Tyn & Gusek, 1990**
Fatty-acid synthase	2300	3.362	17.0	1.230	**Tyn & Gusek, 1990**
Pyruvate dehydrogenase	3780	3.577	12.0	1.079	**Tyn & Gusek, 1990**
Pyruvate dehydrogenase	4800	3.681	12.0	1.079	**Tyn & Gusek, 1990**
Satellite_tobacco_necrosis_virus	9000	3.954	10.7	1.029	**Tyn & Gusek, 1990**
Satellite_tobacco_necrosis_virus	1700	3.230	20.4	1.310	**Tyn & Gusek, 1990**
Turnip_yellow_mosaic_virus	1970	3.294	20.4	1.310	**Tyn & Gusek, 1990**
Turnip_yellow_mosaic_virus	3013	3.479	15.1	1.179	**Tyn & Gusek, 1990**
Turnip_yellow_mosaic_virus	3100	3.491	15.1	1.179	**Tyn & Gusek, 1990**
Alfalfa_mosaic_virus_(top)	3500	3.544	15.1	1.179	**Tyn & Gusek, 1990**
Bacteriophage_MS2_(native_protein)	3770	3.576	15.5	1.190	**Tyn & Gusek, 1990**
BacteriOphage fr	3600	3.556	16.0	1.204	**Durchslag & Zipper, 1997**
Bacteriophage_virus_R17	3620	3.559	14.0	1.146	**Tyn & Gusek, 1990**
Bacteriophage_virus_R17	3600	3.556	13.3	1.123	**Tyn & Gusek, 1990**

Bacteriophage_virus_R17	3700	3.568	13.3	1.123	**Tyn & Gusek, 1990**
Wild_cucumber_mosaic_virus_top_a	4190	3.622	13.3	1.123	**Tyn & Gusek, 1990**
Wild_cucumber_mosaic_virus_top_b	4000	3.602	12.9	1.111	**Tyn & Gusek, 1990**
Wild_cucumber_mosaic_virus_top_b	4300	3.633	12.9	1.111	**Tyn & Gusek, 1990**
Bromegrass_mosaic_virus	4400	3.643	12.9	1.111	**Tyn & Gusek, 1990**
Bromegrass_mosaic_virus	4400	3.643	15.5	1.190	**Tyn & Gusek, 1990**
Bromegrass_mosaic_virus	4700	3.672	15.5	1.190	**Tyn & Gusek, 1990**
Broad_bean_mottle_virus	5400	3.732	15.5	1.190	**Tyn & Gusek, 1990**
Broad_bean_mottle_virus	4750	3.677	14.4	1.158	**Tyn & Gusek, 1990**
Broad_bean_mottle_virus	4850	3.686	14.4	1.158	**Tyn & Gusek, 1990**
Broad_bean_mottle_virus	5000	3.699	14.4	1.158	**Tyn & Gusek, 1990**
Broad_bean_mottle_virus	5200	3.716	13.8	1.140	**Tyn & Gusek, 1990**
Turnip_yellow_mosaic_virus	5600	3.748	14.4	1.158	**Tyn & Gusek, 1990**
Turnip_yellow_mosaic_virus	4970	3.696	15.5	1.190	**Tyn & Gusek, 1990**
Turnip_yellow_mosaic_virus	5000	3.699	15.5	1.190	**Tyn & Gusek, 1990**
Tobacco_necrosis_virus	5530	3.743	15.5	1.190	**Tyn & Gusek, 1990**
Tobacco_necrosis_virus	6000	3.778	15.3	1.185	**Tyn & Gusek, 1990**
Southern_bean_mosaic_virus	7400	3.869	14.0	1.146	**Tyn & Gusek, 1990**
Southern_bean_mosaic_virus	6600	3.820	13.9	1.143	**Tyn & Gusek, 1990**
Southern_bean_mosaic_virus	6602	3.820	13.9	1.143	**Tyn & Gusek, 1990**
Southern bean mosaic virus	6630	3.822	13.4	1.127	**Durchslag & Zipper, 1997**
Alfalfa_mosaic_virus_(bottom)	6690	3.825	13.9	1.143	**Tyn & Gusek, 1990**
Alfalfa_mosaic_virus_(bottom)	6820	3.834	11.3	1.053	**Tyn & Gusek, 1990**
Alfalfa_mosaic_virus_(bottom)	6860	3.836	11.3	1.053	**Tyn & Gusek, 1990**
Alfalfa_mosaic_virus_(bottom)	6920	3.840	10.5	1.021	**Tyn & Gusek, 1990**
Tobacco_bushy_stunt_virus	7400	3.869	10.5	1.021	**Tyn & Gusek, 1990**
Bacteriophage_lambda_(enlarged_prehead)	10700	4.029	11.5	1.061	**Tyn & Gusek, 1990**
Bacteriophage_lambda_(processed_prehead)	17000	4.230	6.9	0.839	**Tyn & Gusek, 1990**
Bacteriophage_lambda_(empty_head)	18000	4.255	7.8	0.892	**Tyn & Gusek, 1990**
Bacteriophage_lambda_(unprocessed_head)	21000	4.322	6.4	0.806	**Tyn & Gusek, 1990**
Bacteriophage_lambda_(full_head)	22000	4.342	7.6	0.881	**Tyn & Gusek, 1990**
Lipid-containing_bacteriophage	56000	4.748	6.5	0.813	**Tyn & Gusek, 1990**
Rice dwarf virus	45000	4.653	5.5	0.740	**Durchslag & Zipper, 1997**
ELONGATED, FIBROUS STRUCTURE OR ROD-LIKE CONFORMATION IN AQUEOUS SOLUTION Fitting results of LOG(MW) *vs.* LOG($D_{solvent}$): **Y=A+B·X:** R=-0.990; P<0.0001; A=3.06±0.0542(SE); B=-0.715±0.0173(SE)					

Flagellin	42	1.620	54.0	1.732	**Tyn & Gusek, 1990**
Meromyosin	120	2.079	22.5	1.352	**Tyn & Gusek, 1990**
Fibrinogen	340	2.531	20.2	1.305	**Tyn & Gusek, 1990**
Myosin	493	2.693	11.6	1.064	**Tyn & Gusek, 1990**
Myosin	570	2.756	10.0	1.000	**Tyn & Gusek, 1990**
Myosin	594	2.774	8.7	0.940	**Tyn & Gusek, 1990**
RNA_of_tobacco_mosaic_virus	2150	3.332	7.0	0.843	**Tyn & Gusek, 1990**
DNA	4000	3.602	1.3	0.114	**Tyn & Gusek, 1990**
DNA	5000	3.699	1.3	0.114	**Tyn & Gusek, 1990**
DNA	6000	3.778	1.3	0.114	**Tyn & Gusek, 1990**
p1868	1232	3.091	7.0	0.845	**Prazeres, 2008**
PLN1	1386	3.142	6.0	0.778	**Prazeres, 2008**
Not available	1525	3.183	5.6	0.748	**Prazeres, 2008**
PK3A108	1535	3.186	5.4	0.728	**Prazeres, 2008**
pUC18	1773	3.249	5.4	0.732	**Prazeres, 2008**
pUC8	1793	3.254	4.9	0.690	**Prazeres, 2008**
pUC18-3A108	1847	3.266	4.8	0.681	**Prazeres, 2008**
pGem1a	2462	3.391	4.1	0.614	**Prazeres, 2008**
pBR322	2880	3.459	3.7	0.568	**Prazeres, 2008**
p30delta	3136	3.496	3.5	0.545	**Prazeres, 2008**
pACL29	3564	3.552	3.1	0.491	**Prazeres, 2008**
ColE1	4290	3.632	2.9	0.461	**Prazeres, 2008**
pDR1996	6732	3.828	2.3	0.362	**Prazeres, 2008**
pPIC9K<TRL5>	7326	3.865	1.7	0.217	**Prazeres, 2008**
pCC1FOS™45	29700	4.473	0.6	-0.222	**Prazeres, 2008**
CTD-2342K16	74448	4.872	0.5	-0.310	**Prazeres, 2008**
CTD-2609C22	121110	5.083	0.3	-0.481	**Prazeres, 2008**
CTD-2657L24	189486	5.278	0.2	-0.638	**Prazeres, 2008**
EGFP1	30	1.477	104.0	2.017	**Pack *et al.*, 2006**
EGFP1	27	1.431	87.0	1.940	**Arrio-Dupont *et al.*, 2000**
EGFP2	60	1.778	71.8	1.856	**Pack et al., 2006**
EGFP3	90	1.954	61.3	1.787	**Pack et al., 2006**
EGFP4	120	2.079	48.7	1.688	**Pack et al., 2006**
EGFP5	150	2.176	45.2	1.655	**Pack et al., 2006**
EGFP1	27	1.430	97.3	1.988	**Vámosi *et al.*, 2016**
EGFP2	54	1.735	98.8	1.995	**Vámosi *et al.*, 2016**

EGFP3	82	1.912	60.2	1.780	**Vámosi *et al.*, 2016**
EGFP4	109	2.038	54.8	1.739	**Vámosi *et al.*, 2016**
ELONGATED, FIBROUS STRUCTURE OR ROD-LIKE MOLECULES IN THE NUCLEUS OF HELA CELLS Fitting results of LOG(MW) *vs.* LOG($D_{solvent}$): **Y=A+B·X:** R=-0.926; P=3.42E-4; A=2.72±0.214(SE); B=-0.748±0.115(SE)					
EGFP1 - nucleus HeLa	30	1.477	32.3	1.510	**Pack *et al.*, 2006**
EGFP2 - nucleus HeLa	60	1.778	21.2	1.327	**Pack *et al.*, 2006**
EGFP3 - nucleus HeLa	90	1.954	16.5	1.218	**Pack *et al.*, 2006**
EGFP4 - nucleus HeLa	120	2.079	12.3	1.088	**Pack *et al.*, 2006**
EGFP5 - nucleus HeLa	150	2.176	11.1	1.046	**Pack *et al.*, 2006**
EGFP1 - nucleus HEK293, HeLa, TP366, T98G	27	1.431	50.6	1.704	**Dross *et al.*, 2009**
EGFP2 - nucleus HEK293, HeLa, TP366, T98G	54	1.732	31.0	1.491	**Dross *et al.*, 2009**
EGFP3 - nucleus HEK293, HeLa, TP366, T98G	81	1.908	23.8	1.377	**Dross *et al.*, 2009**
EGFP4 - nucleus HEK293, HeLa, TP366, T98G	108	2.033	20.2	1.305	**Dross *et al.*, 2009**
ELONGATED, FIBROUS STRUCTURE OR ROD-LIKE MOLECULES IN THE CYTOSOL OF HELA CELLS Fitting results of LOG(MW) *vs.* LOG($D_{solvent}$): **Y=A+B·X:** R=-0.984; P=0.00236; A=2.53±0.131(SE); B=-0.665±0.0688(SE)					
EGFP1 - cytosol HeLa	30	1.477	33.3	1.523	**Pack *et al.*, 2006**
EGFP2 - cytosol HeLa	60	1.778	23.4	1.369	**Pack *et al.*, 2006**
EGFP3 - cytosol HeLa	90	1.954	18.7	1.271	**Pack *et al.*, 2006**
EGFP4 - cytosol HeLa	120	2.079	12.8	1.108	**Pack *et al.*, 2006**
EGFP5 - cytosol HeLa	150	2.176	11.8	1.073	**Pack *et al.*, 2006**
ACGFP1 CONCATEMERS IN THE MITOCHONDRIA OF HELA CELLS Fitting results of LOG(MW) *vs.* LOG($D_{solvent}$): **Y=A+B·X:** R=-0.997; P=0.00268; A=2.81±0.0923(SE); B=-0.976±0.0506(SE)					
AcGFP1	29	1.465	23.9	1.378	**Current study**
AcGFP1[2]	58	1.760	11.8	1.072	**Current study**
AcGFP1[3]	88	1.943	8.6	0.934	**Current study**
AcGFP1[4]	115	2.062	6.0	0.780	**Current study**

Remarks: Data in **red** of **Pack *et al.*, 2006** were corrected as proposed by **Dross *et al.*, 2009** using a diffusion constant for Rhodamine 6G of 430 $\mu m^2/s$ (**Jameson *et al.*, 2009**). Data for the Tobacco mosaic virus was not included since this virus is geometrically extreme (*i.e.* it resembles a cylinder with a length/diameter ratio of 16.7; **Saxton, 2014**).

Appendix Supplementary Table S3: Interpretation of the data sets in Appendix Supplementary Table S2

Dataset	Environment	Techniques	Interpretation	References
Globular or spherical conformation in aqueous solution				
Globular	Aqueous solution	Various	Globular structure	**Young *et al.*, 1980** **Tyn & Gusek, 1990** **Durchslag & Zipper, 1997** **Gribbon *et al.*, 1998** **Arrio-Dupont *et al.*, 2000** **Papadopoulos *et al.*, 2000** **He & Niemeyer, 2003** **Saxton, 2014**
Virus	Aqueous solution	Various	Globular structure	**Tyn & Gusek, 1990** **Durchslag & Zipper, 1997** **Saxton, 2014**
Elongated, fibrous structure or rod-like conformation in aqueous solution				
Fibrous	Aqueous solution	Various	Fibrous, elongated structure	**Tyn & Gusek, 1990** **Saxton, 2014**
Plasmids	Aqueous solution	Various	Supercoiled, elongated structure	**Prazeres, 2008**
(E)GFP concatemers	Aqueous solution	FCS	Rod-like molecules	**Pack *et al.*, 2006** **Vámosi *et al.*, 2016**
Elongated, fibrous structure or rod-like molecules in the cell				
EGFP concatemers	Nucleus of HeLa cells	FCS	Rod-like molecules	**Pack *et al.*, 2006**
EGFP concatemers	Cytoplasm of HeLa cells	FCS	Rod-like molecules	**Pack *et al.*, 2006**
EGFP concatemers	Nucleus of HeLa cells	FCS	Rod-like molecules	**Dross *et al.*, 2009**

5. Appendix Supplementary References

1. **Ajaz S**, Czajka A, Malik A (2015) Accurate measurement of circulating mitochondrial DNA content from human blood samples using real-time quantitative PCR. *Meth Mol Biol* 1264: 117-131
2. **Akabayov B**, Akabayov SR, Lee SJ, Wagner G, Richardson CC (2013) Impact of macromolecular crowding on DNA replication. *Nat Commun* 4: 1615
3. **Appelhans T**, Richter CP, Wilkens V, Hess ST, Piehler J, Busch KB (2011) Nanoscale organisation of mitochondrial microcompartments revealed by combining tracking and localization microscopy. *Nano Lett* 12: 610-616
4. **Arrio-Dupont M**, Cribier S, Foucault G, Devaux PF, d'Albis A, (1996) Diffusion of fluorescently labeled macromolecules in cultured muscle cells. *Biophys J* 70: 2327-2332
5. **Arrio-Dupont M**, Foucault G, Vacher M, Devaux PF, Cribier S (2000) Translational diffusion of globular proteins in the cytoplasm of cultured muscle cells. *Biophys J* 78: 901-907
6. **Bell P**, Vandenberghe LH, Wu D, Johnston J, Limberis M, Wilson JM (2007) A comparative analysis of novel fluorescent proteins as reporters for gene transfer studies. *J Histochem Cytochem* 55: 931-939
7. **Blässle A**, Soh G, Braun T, Mörsdorf D, Preiss H, Jordan BM, Müller P (2018) Quantitative diffusion measurements using the open-source software PyFRAP. *Nat Commun* 9: 1582
8. **Burbulla LF**, Fitzgerald JC, Stegen K, Westermeier J, Thost AK, Kato H, Mokranjac D, Sauerwald J, Martins LM, Woitalla D, *et al.* (2014) Mitochondrial proteolytic stress induced by loss of mortalin function is rescued by Parkin and PINK1. *Cell Death Dis* 5: e1180
9. **Bulina ME**, Chudakov DM, Britanova OV, Yanushevich YG, Staroverov DB, Chepurnykh TV, Merzlyak EM, Shkrob MA, Lukyanov S, Lukyanov KA (2006) A genetically encoded photosensitizer. *Nat Biotechnol* 24: 95-99
10. **Bustin SA**, Benes V, Garson JA, Hellemans J, Huggett J, Kubista M, Mueller R, Nolan T, Pfaffl MW, Shipley GL, Vandesompele J, Wittwer CT (2009) The MIQE guidelines: minimum information for publication of quantitative real-time PCR experiments. *Clin Chem* 55: 611-622.
11. **Dashevskaya S**, Kopito RB, Friedman R, Elbaum M, Epel BL (2008) Diffusion of anionic and neutral GFP derivatives through plasmodesmata in epidermal cells of *Nicotiana benthamiana*. *Protoplasma* 234: 13-23.
12. **Dieteren CEJ**, Willems PHGM, Vogel RO, Swarts HG, Fransen J, Roepman R, Crienen G, Smeitink JAM, Nijtmans LGJ, Koopman WJH (2008) Subunits of Mitochondrial Complex I Exist as part of matrix- and membrane-associated subcomplexes in living cells. *J Biol Chem* 283: 34753-34761
13. **Dieteren CEJ**, Gielen SCAM, Nijtmans LGJ, Smeitink JAM, Swarts HG, Brock R, Willems PHGM, Koopman WJH (2011) Solute diffusion is hindered in the mitochondrial matrix. *Proc Natl Acad Sci USA* 108: 8657-8662
14. **Divakaruni AS**, Jastroch M (2022) A practical guide for the analysis, standardization and interpretation of oxygen consumption measurements. *Nat Metab* 4:978-994
15. **Dross N**, Spriet C, Zwerger M, Müller G, Waldeck W, Langowski J (2009) Mapping eGFP oligomer mobility in living cell nuclei. *PLoS ONE* 4: e5041
16. **Durchslag H**, Zipper P (1997) Prediction of hydrodynamic parameters of biopolymers from small-angle scattering data. *J Appl Cryst* 30: 1112-1124
17. **Einstein A** (1905) Über die von der molekularkinetischen Theorie der Wärme geforderte Bewegung von in ruhenden Flüssigkeiten suspendierten Teilchen. *Annalen der Physik* 322: 549-560
18. **Elachouri G,** Vidoni S, Zanna C, Pattyn A, Boukhaddaoui H, Gaget K, Yu-Wai-Man P, Gasparre G, Sarzi E, Delettre C, *et al.* (2011) OPA1 links human mitochondrial genome maintenance to mtDNA replication and distribution. *Genome Res* 21: 12-20
19. **Erban R** (2014) From molecular dynamics to Brownian dynamics. *Proc R Soc A* 470: 20140036
20. **Goodwin JS**, Kenworthy AK (2005) Photobleaching approaches to investigate diffusional mobility and trafficking of Ras in living cells. *Methods* 37: 154-164
21. **Gribbon P**, Hardingham TE (1998) Macromolecular diffusion of biological polymers measured by confocal fluorescence recovery after photobleaching. *Biophys J* 75: 1032-1039

22. **He L**, Niemeyer B (2003) A novel correlation for protein diffusion coefficients based on molecular weight and radius of gyration. *Biotechnol Prog* 19: 544-548
23. **Houtkooper RH,** Mouchiroud L, Ryu D, Moullan N, Katsyuba E, Knott G, Williams RW, Auwerx J (2013) Mitonuclear protein imbalance as a conserved longevity mechanism. *Nature* 497: 451-459
24. **Huber GA, McCammon JA** (2019) Brownian dynamics simulations of biological molecules. *Trends Chem* 1: 727-738
25. **Hu C**, Shu L, Huang X, Yu J, Li L, Gong L, Yang M, Wu Z, Gao Z, Zhao Y, Chen L, Song Z (2020) OPA1 and MICOS regulate mitochondrial crista dynamics and formation. *Cell Death Dis* 11: 940
26. **Jameson DM**, Ross JA, Albanesi JP (2009) Fluorescence fluctuation microscopy: ushering a new age of enlightenment for cellular dynamics. *Biophys Rev* 1: 105-118
27. **Koopman WJH**, Visch HJ, Smeitink JAM, Willems PHGM (2006) Simultaneous, quantitative measurement and automated analysis of mitochondrial morphology, mass, potential and motility in living human skin fibroblasts, *Cytometry A* 69A: 1-12
28. **Koopman WJH**, Distelmaier F, Hink MA, Verkaart S, Wijers M, Fransen J, Smeitink JAM, Willems PHGM (2008a) Inherited complex I deficiency is associated with faster protein diffusion in the matrix of moving mitochondria. *Am J Physiol Cell Physiol* 294: C1124-C1132
29. **Koopman WJH,** Distelmaier F, Esseling JJ, Smeitink JAM, Willems PHGM (2008b) Computer-assisted live cell analysis of mitochondrial membrane potential, morphology and calcium handling. *Methods* 46: 304-311
30. **Lavalette D**, Hink MA, Tourbez M, Tétreau C, Visser AJ (2006) Proteins as microviscosimeters: Brownian motion revisited. *Eur Biophys J* 35: 517-522
31. **Levenberg K** (1944) A method for the solution of certain non-linear problems in least squares. *Quarterly Appl Math* 2: 164-168.
32. **Lorén N**, Hagman J, Jonasson JK, Deschout H, Bernin D, Cella-Zanacchi F, Diaspro A, McNally JG, Ameloot M, Smisdom N, (2015) Fluorescence recovery after photobleaching in material and life sciences: putting theory into practice. *Q Rev Biophys* 48: 323-387
33. **Malik AN**, Shahni R, Rodriguez-de-Ledesma A, Laftah A, Cunningham P (2011) Mitochondrial DNA as a non-invasive biomarker: accurate quantification using real time quantitative PCR without co-amplification of pseudogenes and dilution bias. *Bioch Biophys Res Comm* 412 :1-7
34. **Marquardt DW** (1963) An algorithm for the least-squares estimation of nonlinear parameters. *SIAM J Appl Math.* 11: 431-441.
35. **Minier F**, Sigel E (2004) Techniques: Use of concatenated subunits for the study of ligand-gated ion channels. *Trends Pharmacol Sci* 25: 499-503
36. **Monkos K** (2004) On the hydrodynamics and temperature dependence of the solution conformation of human serum albumin from viscometry approach. *Biochim Biophys Acta* 1700: 27-34
37. **Minton AP** (1981) Excluded volume as a determinant of macromolecular structure and reactivity. *Biopolymers* 20: 2093-2120
38. **Moullan N,** Mouchiroud L, Wang X, Ryu D, Williams EG, Mottis A, Jovaisaite V, Frochaux MV, Quiros PM, Deplancke B, *et al.* (2015) Tetracyclines disturb mitochondrial function across eukaryotic models: a call for caution in biomedical research. *Cell Rep* 10: 1681-1691
39. **Nooteboom M**, Forkink M, Willems PHGM, Koopman WJH (2012) Live-cell quantification of mitochondrial functional parameters. Chapter 6 in: *Neuromethods* 70: Visualization techniques, from immunohistochemistry to Magnetic Resonance Imaging (Badoer, E., ed.)
40. **Nicholls TJ,** Gustafsson CM (2018) Separating and segregating the human mitochondrial genome. *Trends Biochem Sci* 43: 869-881
41. **Ölveczky BP,** Verkman AS (1998) Monte Carlo analysis of obstructed diffusion in three dimensions: application to molecular diffusion in organelles. *Biophys J* 74: 2722-2730
42. **Pack C**, Saito K, Tamura M, Kinjo M (2006) Microenvironment and effect of energy depletion in the nucleus analyzed by mobility of multiple oligomeric EGFPs. *Biophys J* 91: 3921-3936

43. **Palmer AE**, Jin C, Reed JC, Tsien RY (2004) Bcl-2-mediated alterations in endoplasmic reticulum Ca^{2+} analyzed with an improved genetically encoded fluorescent sensor. *Proc Natl Acad Sci USA* 101: 17404-17409
44. **Papadopoulos S**, Jürgens KD, Gros G (2000) Protein diffusion in living skeletal muscle fibers: Dependence on protein size, fiber type, and contraction. *Biophys J* 79: 2084-2094
45. **Partikian A**, Olveczky B, Swaminathan R, Li Y, Verkman AS (1998) Rapid diffusion of green fluorescent protein in the mitochondrial matrix. *J Cell Biol* 140: 821-829
46. **Perrin, F.** (1936) Mouvement Brownien d'un ellipsoide (II). Rotation libre et dépolarisation des fluorescences. Translation et diffusion de molécules ellipsoidales. *J Phys Radium* 7: 1-11
47. **Prazeres DMF** (2008) Prediction of diffusion coefficients of plasmids. *Biotechnol Bioeng* 99:1040-1044
48. **Richter U,** Ng KY, Suomi F, Marttinen P, Turunen T, Jackson C, Suomalainen A, Vihinen H, Jokitalo E, Nyman TA, *et al.* (2019) Mitochondrial stress response triggered by defects in protein synthesis quality control. *Life Sci Alliance* 2: e201800219
49. **Rizzutto F,** Nakase H, Darras B, Francke U, Fabrizi GM, Mengel T, Walsh F, Kadenbach B, DiMauro S, Schon EA (1989) A gene specifying subunit VIII of human cytochrome-*c* oxidase is localized to chromosome 11 and is expressed in both muscle and non-muscle tissues. *J Biol Chem* 264: 10595–10600
50. **Saxton MJ** (2014) Wanted: Scalable tracers for diffusion measurements. *Phys Chem B* 118: 12805-12817
51. **Segawa M**, Wolf DM, Hultgren NW, Williams DS, van der Bliek AM, Schackelford DB, Liesa M, Shirihai OS. (2020) Quantification of cristae architecture reveals time-dependent characteristics of individual mitochondria. *Life Sci Alliance* 3: e201900620
52. **Shpilka T,** Haynes CM (2018) The mitochondrial UPR: mechanisms, physiological functions and implications in ageing. *Nat Rev Mol Cell Biol* 19: 109-120
53. **Sutherland W** (1905) A dynamical theory of diffusion for non-electrolytes and the molecular mass of albumin. *Philosophical Magazine* 9: 781–785
54. **Terry BR**, Matthews EK, Haseloff J. (1995) Molecular characterisation of recombinant green fluorescent protein by fluorescence correlation microscopy. *Biochem Biophys Res Commun* 217: 21-27
55. **Thubron EB**, Rosa HS, Hodges A, Sivaprasad S, Francis PT, Pienaar IS, Malik AN (2019) Regional mitochondrial DNA and cell-type changes in post-mortem brains of non-diabetic Alzheimer's disease are not present in diabetic Alzheimer's disease. *Sci Rep* 9: 11386
56. **Tyn MT**, Gusek TD (1990) Prediction of diffusion coefficients of proteins. *Biotechnol Bioeng* 35: 327-338
57. **Van Helvoort JMLM,** Kool J, Woldringh CL (1996) Chloramphenicol causes fusion of separated nucleoids in *Escherichia coli* K-12 cells and filaments. *J Bacteriol* 178: 4289-4293
58. **Vámosi G**, Mücke N, Müller G, Krieger JW, Curth U, Langowski J, Tóth K (2014) EGFP oligomers as natural fluorescence and hydrodynamic standards. *Sci Rep* 6: 33022
59. **Von Smoluchowski M** (1906) Zur kinetischen Theorie der Brownschen Molekularbewegung und der Suspensionen. *Annalen der Physik* 326: 756–780
60. **Weissert V**, Rieger B, Morris S, Arroum T, Psathaki OE, Zobel T, Perkins G, Busch KB (2021) Inhibition of the mitochondrial ATPase function by IF1 changes the spatiotemporal organisation of ATP synthase. *Biochim Biophys Acta Bioenerg* 1862: 148322
61. **Wilkens V**, Kohl W, Busch K (2012) Restricted diffusion of OXPHOS complexes in dynamic mitochondrial delays their exchange between cristae and engenders a transitory mosaic distribution. *J Cell Sci* 126: 103-116
62. **Willems PHGM**, Swarts HG, Hink MA, Koopman WJH (2009) Chapter 16: The use of fluorescence correlation spectroscopy to probe mitochondrial mobility and intramatrix protein diffusion. *Methods Enzymol* 456: 287-302

63. **Wolf DM**, Segawa M, Kondadi AK, Anand R, Bailey ST, Reichert AS, van der Bliek AM, Schackelford DB, Liesa M, Shirihai O (2019) Individual cristae within the same mitochondrion display different membrane potentials and are functionally independent. *EMBO J* 38: e101056
64. **Xu M,** Bi X, He X, Yu X, Zhao M, Zhang W (2016) Inhibition of the mitochondrial unfolded protein response by acetylcholine alleviated hypoxia/reoxygenation-induced apoptosis of endothelial cells. *Cell Cycle* 15: 1331-1343
65. **Yang F**, Moss LG, Philips Jr, GN (1996) The molecular structure of green fluorescent protein. *Nature Biotechnol* 14: 1246-1251
66. **Young ME**, Carroad PA, Bell RL (1980) Estimation of diffusion coefficients of proteins. *Biotechnol Bioeng* 22: 947-955
67. **Zhao Q,** Wang J, Levichkin IV, Stasinopoulos S, Ryan MT, Hoogenraad NJ (2002) A mitochondrial specific stress response in mammalian cells. *EMBO J* 21: 4411-4419